Department of Physics and Astronomy

Heidelberg University

Master thesis

in Physics

submitted by

Nils Becker

born in Ludwigshafen am Rhein

2023

Self-similar scaling in One-Dimensional Exciton-Polariton Condensates governed by Kardar–Parisi–Zhang Dynamics

This Master thesis has been carried out by Nils Becker

at the

Kirchhoff-Institut für Physik

under the supervision of

Herrn Prof. Thomas Gasenzer

Zusammenfassung

In der vorliegenden Arbeit wird die Dynamik eines eindimensionalen Exziton-Polariton-Kondensats untersucht, bei dem die Phasenfluktuationen durch die Kardar-Parisi-Zhang-Gleichung bestimmt sind. Wir analysieren die Defekte, die in der zeitlichen Entwicklung des Kondensats auftreten und vergleichen ihre Dichteprofile mit denen eines Solitons. Durch die Beobachtung von Phasensprüngen an den Defektpositionen sind wir in der Lage, diese als dunkle Solitonen zu klassifizieren. Wenn wir unseren Fokus auf die Defektwechselwirkungen verlagern, können wir an den Schnittpunkten der Solitonen die Entstehung von wirbelartigen Strukturen in der Zeit-Raum-Ebene beobachten. Eine Untersuchung der Impulsbesetzungszahlen zu verschiedenen Zeitpunkten zeigt ein bemerkenswertes Skalierungsverhalten von einer anfänglich kastenförmigen Verteilung hin zu einem Potenzgesetzabfall. Der Exponent κ dieses Abfalls ist ungewöhnlich hoch. Sein Wert reicht von etwa 4 bis 7 und hängt stark mit der Lebensdauer der Solitonen im Kondensat zusammen. Um die Selbstähnlichkeit des Skalierungsverhaltens zu bestätigen, führen wir eine Reskalierung der Besetzungsspektren bezüglich einer Referenzzeit durch. Aus diesem Reskalierungsprozess können Skalierungsexponenten nahe $\frac{1}{3}$ für α und β abgeleitet werden. Aus der Selbstähnlichkeit der Skalierung schließen wir, dass sich das Polaritonkondensat in der Nähe eines nicht-thermischen Fixpunktes befindet.

Abstract

In this thesis we study the dynamics of a one-dimensional exciton-polariton condensate, where the phase fluctuations are governed by the Kardar-Parisi-Zhang equation. We analyse the defects that emerge as the condensate evolves and compare their density profiles to those of a soliton. By observing phase jumps at the defect positions, we are able to classify them as dark solitons. Shifting our focus to defect interactions, we reveal the emergence of vortex-like structures in the time-space plane at the soliton intersection points. An examination of the momentum occupation number at different times reveals a remarkable scaling behaviour, from an initial box-like distribution to a power law decay. The power law exponent κ is found to be anomalously high, ranging from about 4 to 7, and its value is strongly related to the lifetime of the solitons present in the system. To validate the self-similarity of this scaling behaviour, we perform a rescaling of the occupation spectra with respect to a reference time. Scaling exponents close to $\frac{1}{3}$ for both α and β are extracted from this rescaling process. We conclude that the polariton condensate is close to a non-thermal fixed point based on the self-similarity of the scaling.

Contents

1 Introduction

Polaritons are at the forefront of modern research in solid state physics. These quasiparticles, composed of photons and electron-hole pairs, form at the boundary between light and matter. Due to their bosonic nature and low mass, which is only a fraction of the mass of an electron, they are able to condense into a Bose-Einstein state even at relatively high temperatures. After the first successful condensation a decade ago, current research achieved progress in lower-dimensional polariton condensates coupled to excitonic reservoirs. Recent publications have revealed a close connection between the dynamics of one-dimensional polariton condensates and the Kardar-Parisi-Zhang (KPZ) equation.

Against this scientific background, this thesis examines the subject of polariton condensates, with a specific emphasis on the study of their dynamics. In experimental settings where light cannot be retained indefinitely, constant replenishment of polaritons is upheld via laser beam pumping. Therefore, polariton condensates serve as a prime example of driven dissipative systems that exist in an out-of-equilibrium state. This provides a unique opportunity to examine various theoretical predictions, in particular those regarding universal dynamics in far-from-equilibrium scenarios.

One of the powerful tools developed for the study of non-equilibrium systems is the concept of universal non-thermal fixed points (NTFPs). The strength of this concept lies in its ability to describe the dynamics of various systems using only a few macroscopic parameters by classifying them into specific universality classes [1, 2]. At its core, the idea of NTFPs arises from the empirical observation that systems far from equilibrium, on their way to thermal equilibrium, eventually pass through a regime characterised by significantly slowed down dynamics. This regime is closely related to the proximity of the system to a stationary nonequilibrium state associated with an NTFP. The critically slowed dynamics are characterised by a self-similar spatio-temporal evolution of the order parameter correlation functions [3, 4, 5, 6], resembling critical phenomena in equilibrium where a fixed point acts as a universal attractor in the framework of renormalisation group theory.

Crucially, this universal behaviour is independent of specific initial conditions, allowing the classification of physical systems into universality classes, each defined by a unique set of universal scaling exponents. The advantage of this approach is now that all systems falling within a given universality class exhibit the same macroscopic behaviour. As a result, the time evolution of a system is decoupled from its microscopic details. This phenomenon offers a remarkable opportunity to understand and predict the real-time evolution of diverse systems, ranging from quark-gluon plasmas in quantum chromodynamics [7] to the post-inflationary dynamics of the early universe [8], by studying a more experimentally accessible system within the same universality class.

The focus of this work is the numerical simulation of a one-dimensional polariton condensate coupled to an excitonic reservoir, the system in which the connection to the KPZ equation was first established. We study different parameter regimes, exploring the dynamics of the system and the intricate patterns that emerge during its time evolution. In order to ascertain our proximity to a non-thermal fixed point, we examine the correlation functions, in particular the momentum occupation number, for evidence of self-similar scaling.

The subsequent chapters of this thesis are organized as follows: In chapter 2, we introduce the theoretical concepts central to this thesis. We begin with an examination of the phenomenon of Bose-Einstein Condensation (BEC). As a mathematical framework, we introduce the Gross-Pitaevskii model in section 2.2 and discuss vortices as prominent solutions within this mean-field framework. In section 2.3, our focus shifts to the primary physical system studied in this thesis: polariton condensates. We explore the intricate interplay between photons and excitons that gives rise to polaritons, as well as the experimental setups, such as microcavities, used to study them. Section 2.4 includes a discussion of universal dynamics and non-thermal fixed points, as well as the application of renormalisation group theory to extract scaling exponents characterising critical behaviour. In section 2.5, we revisit the connection between KPZ universality and the polariton model, as discussed in [9], by using a fluctuation ansatz for the equations describing the mean-field behaviour. Chapter 3 presents the essential numerical tools and techniques employed in our simulations. We begin by addressing the discretisation of continuous equations of motion in section 3.1. Additionally, this section also covers the conversion from physical units to numerical ones. Subsequently, we present the split-step Fourier algorithm in the following section, which serves as our method to computing the time evolution of the discretised equations of motion. In section 3.3, the truncated

Wigner approximation is introduced as a semi-classical technique to incorporate quantum effects. This is accomplished by adding noise to the initial state and averaging over several simulation runs.

Chapter 4 presents the results of our numerical simulations, which are divided into two distinct sections, each representing different parameter regimes. In the first section we study the emergence of defects during the time evolution of the condensate. Our analysis focuses on their density profiles and compares them to the characteristics of dark solitons. In addition, we study the phase structures that arise when these defects collide, revealing phase windings in the time-space plane similar to vortices.

In section 4.2 we turn our attention to the dynamics of the system. We confirm the presence of a non-thermal fixed point by studying the momentum occupation numbers at different time points. The occupation spectrum undergoes a clear transformation, changing from an initial box-like distribution to a power law decay. We discuss the anomalously high power law exponents, which also depend on the lifetime of the solitonic defects in the system. To validate the self-similarity of the scaling behaviour, we perform a rescaling of the occupancy spectra relative to a reference time and subsequently examine the extracted scaling exponents.

We conclude in chapter 5 with an outlook on promising avenues for further research. In particular, we highlight the potential connection between the KPZ-driven exciton-polariton condensate and other low-temperature systems.

2 Theoretical Background

2.1 Bose-Einstein Condensates

Sometimes referred to as the fifth state of matter, Bose-Einstein condensates (BEC) form when the interatomic distances of a dilute bosonic gas become comparable to its thermal de Broglie wavelength. At this point, the wave functions of the individual bosons begin to overlap, causing the gas to undergo a phase transition in which the vast majority of bosons occupy the lowest energy state. Because bosons are indistinguishable, the condensed gas can be described by a single, macroscopic wave function. The condensate thus exhibits a mixture of quantum mechanical and hydrodynamic properties, giving rise to new exotic features such as superfluidity or long-range order. Historically, the concept of Bose-Einstein condensation was proposed by Einstein in 1925 [10], but a real BEC could not be produced until 1995, when the groups of Cornell, Wieman and Ketterle achieved condensation in rubidium and sodium atoms, earning them the Nobel Prize in Physics [11, 12]. The main obstacle to experimental realisation has been the low critical temperatures of a few nanokelvins required for condensation to occur. For an ideal Bose-Einstein condensate, the critical temperature is given by:

$$T_C = \frac{2\pi\hbar^2}{m}\left(\frac{n}{2.612}\right)^{\frac{2}{3}}. \tag{2.1}$$

In order to achieve higher critical temperatures, it is therefore necessary either to reduce the mass of the bosons or to increase their density. Consequently, as early as 1962 excitons, electron hole pairs held together by the Coulomb force, were proposed as a possible solution [13]. These quasiparticles are bosonic by nature and much lighter than atoms, thus forming condensates at significantly higher temperatures. Unfortunately, trapping excitons and forming a condensate presents its own experimental challenges, and no exciton condensates have yet been realised. The breakthrough came with the demonstration of strong coupling between excitons and photons giving rise to polaritons, which are four orders of magnitude lighter than excitons, theoretically enabling the creation of BECs at room temperature [14]. In addition, their dispersion can act as a trap in momentum space. The first irrefutable evidence for a polartion condensate was reported by Kaspraz and Richard in 2006 [15], just ten years after the observation of BECs in atomic clouds.

2.2 Gross-Pitaevskii model and the vortex solution

The mathematical treatment of a generic BEC is a complex undertaking, but simplifies considerably in certain limits, where mean field theory can be applied and the condensate can be described by a nonlinear Schrödinger equation. In this so-called Gross-Pitaevskii model, it is assumed that all bosons of the condensate are in the ground state, so that the BEC can be described by a unique wave function. It is also assumed that the de Broglie wavelength is much longer than the boson-boson interaction range, in order to approximate the bosonic scattering processes by s-wave scattering. Both assumptions are well fulfilled at ultracold temperatures, giving a relatively good description of the behaviour of atomic BECs [16]. In its U(N)-symmetric form, the Lagrangian of the Gross-Pitaevskii model reads:

$$\mathcal{L}_{GP} = \frac{i}{2}(\psi_a^* \partial_t \psi_a - \psi_a \partial_t \psi_a^*) - \frac{1}{2m} \nabla \psi_a^* \cdot \nabla \psi_a - \frac{g}{2}(\psi_a^* \psi_a)^2 \tag{2.2}$$

where ψ is the condensate wave function, the coupling constant g is a function of the s-wave scattering length, and summation over all N fields is implied. The equations of motion of the N ground state wave functions can be extracted from the Euler-Lagrange equations:

$$i\partial_t \psi_a = (-\frac{1}{2m}\Delta + g(\psi_b \psi_b^*)^2)\psi_a. \tag{2.3}$$

This non-linear Schrödinger equation is known as the Gross-Pitaevskii equation (GPE) and determines the behaviour of a condensate at the mean field level. There exist a few analytical solutions, such as the soliton in one dimension. In two dimensions, the Gross-Pitaevskii equation can be solved by a vortex using the following ansatz for the wave function:

$$\psi = \sqrt{\rho_0} f(r) e^{iq\varphi} e^{-i\omega t} \tag{2.4}$$

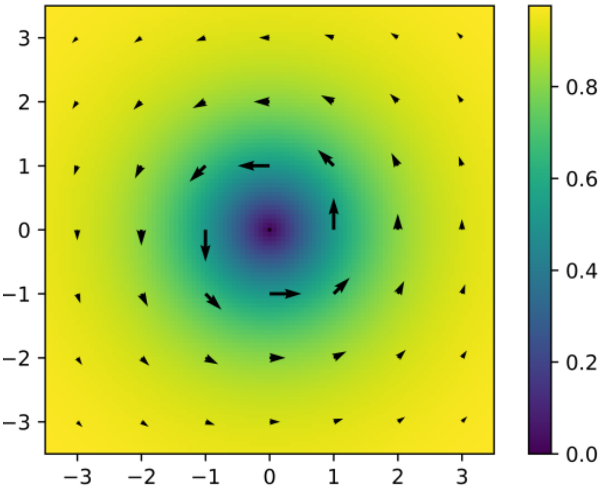

Figure 2.1: Density profile (normalised to the bulk density) and velocity field of a vortex. Figure taken from [17]

where q is the vortex charge and ρ_0 is the bulk density outside the vortex. Plugging the ansatz into the GPE yields:

$$\frac{\partial^2 f}{\partial r^2} + \frac{1}{r}\frac{\partial f}{\partial r} - \frac{q^2}{r^2} f + 2m\omega f - 2mg\rho_0 f^3 = 0. \tag{2.5}$$

Requiring the density far from the vortex to be ρ_0, enforces $f \to 1$ for $r \to \infty$ or equivalently $\omega = g\rho_0$. By introducing the healing length $\xi = 1/\sqrt{2mg\rho_0}$ as the length scale at which the density returns from $\rho = 0$ in the centre to the bulk density ρ_0 and is thus "healed", one can form dimensionless variables $x = r/\xi$ and rewrite the equation as follows:

$$f'' + \frac{1}{x} f' - \frac{q^2}{x^2} f + f - f^3 = 0. \tag{2.6}$$

This equation has no analytical solution but can be evaluated numerically. One finds the characteristic density dip in the centre and a return to the bulk density after ξ. The density profile and velocity field of a condensate around a vortex is shown in Figure 2.1

$$\mathbf{v} \equiv \frac{\mathbf{j}}{\rho} = \frac{q}{mr} \mathbf{e}_{\varphi}. \tag{2.7}$$

In two dimensions, vortices are a crucial phenomenon for describing condensates and their behaviour. They can scatter, form bound vortex-antivortex pairs or annihilate.

The existence of these bound states plays a crucial role, for example, in the Berezinskii–Kosterlitz–Thouless (BKT) transition [18]. In three dimensions, vortices cannot exist, but instead there are tube-like topological defects called vortex tubes. Like their two-dimensional counterparts, they strongly influence the condensate dynamics [19].

2.2.1 Vortices in one dimension

At first glance, the concept of vortices makes little sense in one dimension, since they are topological objects and therefore require at least two dimensions to exist. However, this is not the whole truth, as one can look at the dynamics and take time itself as the second dimension. In this sense, vortices in one-dimensional condensates would be space-time vortices and should appear in a space-time diagram. Unfortunately, there is another problem with this type of object, as it does not solve the Gross-Pitaevski equation. Making a hydrodynamic ansatz

$$\psi = \sqrt{\rho(t,x)}e^{i\theta(t,x)} \tag{2.8}$$

and plugging it into the GPE gives rise to two sets of equations:

$$\partial_t \rho + \frac{1}{m}\partial_x(\rho\partial_x\theta) = 0 \tag{2.9}$$

$$\partial_t \theta = \frac{1}{2m}[\frac{1}{\sqrt{\rho}}\partial_x^2\sqrt{\rho} - (\partial_x\theta)^2] - g\rho. \tag{2.10}$$

For a vortex solution, the density should only be a function of $r = \sqrt{x^2+t^2}$, while the phase should only depend on $\varphi = \arctan(t/x)$. This reduces the two equations to:

$$0 = \sin\varphi\partial_r\rho + \frac{1}{m}[\cos\varphi\partial_r\rho \cdot (-\frac{\sin\varphi}{r}\partial_\varphi\theta) + \rho(\frac{2\cos\varphi\sin\varphi}{r^2}\partial_\varphi\theta + \frac{(\sin\varphi)^2}{r^2}\partial_\varphi^2\theta)] \tag{2.11}$$

$$(1 - \frac{\cos\varphi\partial_\varphi\theta}{mr})\partial_r\rho = -\frac{\rho}{r^2}(2\cos\varphi\partial_\varphi\theta + \sin\varphi\partial_\varphi^2\theta) \tag{2.12}$$

which can be combined into a single differential equation with the analytic solution:

$$\rho(r) = c \cdot (1 - \frac{a}{r})^{-\frac{b}{a}} \tag{2.13}$$

$$a = \frac{\cos\varphi \partial_\varphi \theta}{m} \tag{2.14}$$

$$b = 2\cos\varphi\partial_\varphi\theta + \sin\varphi\partial_\varphi^2\theta \tag{2.15}$$

For ρ to be only r-dependent, the phase must be a constant, which is incompatible with a vortex solution. Thus a normal 1-d Bose gas has no space-time vortices. However, space-time vortices have been observed in several more complex systems. For example, in spin-1 condensates after a quench, they appear to influence the dynamics [20]. More recently, space-time vortices have been observed in polariton condensates [21]. In the next section, the nature of polaritons is explained in more detail.

2.3 Polariton Bose-Einstein condensates

Traditionally, our perceptions of light and matter are very different. While we associate light with a wave or a massless photon that never stops moving, matter around us is subject to friction and tends to stand still. This is why we can put matter in a box and keep it there, whereas the same concept seems unnatural for light. This supposed duality is resolved by the concept of Quantum Fluid of Lights (QFL), which combines concepts from condensed matter physics and optics. For photons to act as a fluid, they must acquire an effective mass and a significant interaction strength, both of which can be achieved by confinement. Confining a photon between two planar mirrors leads to a discritisation of its wave vector along the direction of the cavity

$$k_z L = N\pi. \tag{2.16}$$

Assuming only a small transverse momentum, one can perform a Taylor expansion of the normal dispersion and derive a parabolic relation for the photon

$$\omega(k) = ck \approx ck_z(N) + \frac{c}{2k_z(N)}k_{||}^2. \tag{2.17}$$

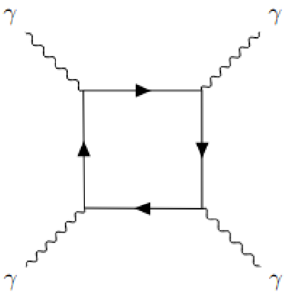

Figure 2.2: Basic Photon-Photon interaction by mediating a virtual electron-positron pair

This dispersion is similar to that of a relativistic particle and gives the photon an effective mass

$$mc^2 = \hbar\omega(k_{||} = 0) = \hbar c k_z. \tag{2.18}$$

Regarding the interaction, the Feynman diagram associated with photon-photon scattering is shown in Fig. 2.2, and the corresponding scattering cross section is proportional to:

$$\sigma \sim \alpha^4 \Big(\frac{h}{m_{el}c}\Big)\Big(\frac{\hbar\omega}{m_{el}c^2}\Big). \tag{2.19}$$

Although possible, the direct interaction between two photons is strongly suppressed not only by the electric fine structure constant, but also by the energy denominator corresponding to the rest mass of the produced electron-positron pair. At typical energies of visible light in the eV range, this gives a huge suppression factor of 10^{-11}. To obtain a significant interaction, we look at the interaction between photons and excitons. Heuristically speaking, the electron-hole pair forming an exciton behaves similarly to an electron-positron pair, resulting in a huge enhancement of the interaction strength.

In this case, the Hamiltonian describing the system of excitons and photons acquires a mixing term. Diagonalising the Hamiltonian leads to two new eigenstates describing a new quasiparticle that contains the properties of both photons and excitons and is known as a polariton. To distinguish between the two polariton eigenstates, they are referred to as the lower and upper branches. By detuning, polaritons can be made more photon-like or more exciton-like.

However, confining quasiparticles for extended periods of time remains an experi-

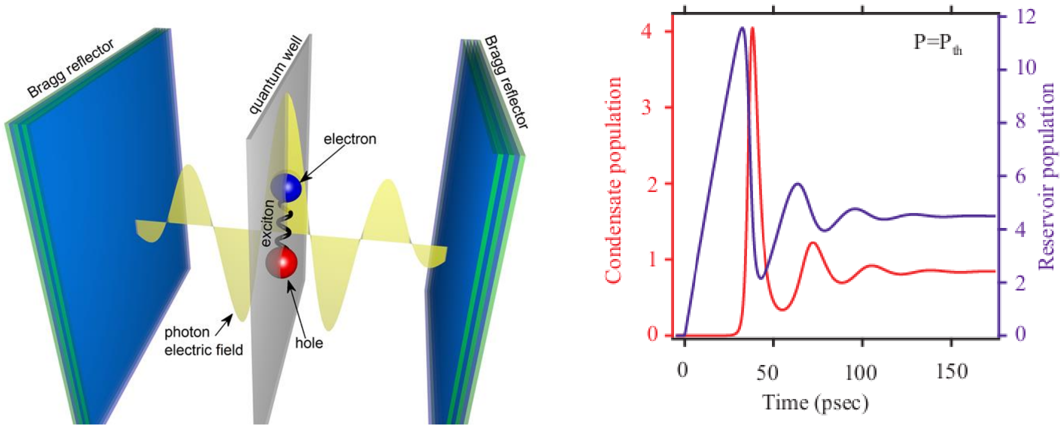

Figure 2.3: Left: A visual representation of a microcavity, in which the Bragg reflectors reflect light, creating a standing wave. Within this cavity, a quantum well is embedded, serving as an active material capable of generating excitons, which subsequently merge with the light wave to form polaritons. Image taken from the Sheffield LDSD group. Right: A plot illustrating the typical population dynamics of a polariton condensate coupled to an exciton reservoir. Plot taken from [14].

mental challenge. From laser physics originates the concept of VCSELS, which are planar microresonators with embedded quantum wells. Unfortunately, their low reflectivity makes them suitable only for the weak coupling regime, where the emission of photons by excitons is irreversible. In the strong coupling regime, Bragg reflectors are used, which have a refraction index of more than 99.9% and, as an added bonus, the hull serves as an active medium for the creation of exitons. In modern experiments, a quantum well is embedded in the cavity, which makes the excitons more robust and enhances the interaction by a factor of about 4. Despite this incredibly high reflectivity, microcavities are subject to losses. They therefore require constant replenishment to be stable, making them a driven dissipative system. Such systems can be described by a generalised Gross-Pitaevskii equation. In the case of the exciton-polariton condensate, there is an additional equation coupled to the GPE that describes the behaviour of an exciton reservoir. Initially, the polariton condensate and the exciton reservoir are empty. To create polaritons, the reservoir is filled by pumping with a laser. When a threshold is reached, the excitons relax into the polariton condensate by stimulated scattering. This cycle is repeated several times until an equilibrium between pump and decay rate is reached (see Fig. 2.3).

$$\begin{aligned}
i\frac{\partial}{\partial_t}\Psi(x,t) =&\Big[\frac{k^2}{2m} - \frac{i}{2}(\gamma_0 + \gamma_2 k^2) + g|\Psi(x,t)|^2 + 2g_R n_R + \frac{i}{2}Rn_R\Big]\Psi(x,t) \\
&+ \xi(x,t) \qquad (2.20)\\
\frac{\partial}{\partial_t}n_R(x,t) =&P - (\gamma_R + R|\Psi(x,t)|^2)n_R(x,t) \qquad (2.21)
\end{aligned}$$

The exciton reservoir with density $n_R(x,t)$ is pumped at rate $P(x)$. Excitons either relax into the polariton condensate by stimulated scattering at rate R or decay via other channels at rate γ_R. Polaritons interact with themselves or with reservoir excitons, where g and g_R are the polariton-polariton and polariton-exciton interaction strengths, respectively. γ_0 and γ_2 describe the in general momentum dependent decay of the polariton condensate field Ψ. Finally, $\xi(x,t)$ is a Gaussian noise induced by drive and loss.

In addition to microcavities, there is another platform for studying this particular physics, namely propagating geometries. This system uses the formal analogy between the generalised GPE and light propagating in a bulk medium, where the z-coordinate than takes on the role of time. We will not go into this approach in detail, in the following we will follow the classic microcavity approach, but the interested reader can refer to [22]. QFLs are not only of interest for technical applications, as their ability to form condensates near room temperature could open the door to many new applications, but they are also prime examples of many-body physics in the non-equilibrium regime, making them an interesting object of study in this field of physics.

2.4 Universal scaling dynamics far from equilibrium

In this section we want to take a closer look at the universal scaling dynamics of quantum many-body systems far from equilibrium and the closely related concept of non-thermal fixed points. The observation of universal dynamics in equilibrium systems is an important result from statistical mechanics. Universality in this context means that a wide variety of very different systems behave similarly close to a phase transition. This manifests itself in a critical exponent corresponding to a universality class. The phenomenon can be understood with the help of renormalisation group theory. The basic idea of the renormalisation group approach is to study a physical system under different spatial resolutions. It turns out that in the vicinity of a phase transition, the correlation functions of the system look the same regardless of the chosen resolution. Shifting the resolution by a factor s then leads to a rescaling of the correlators $C(x, s)$ between points with spatial separation x according to $C(x, s) = s^{\zeta} f_s(x/s)$. This implies that the correlator depends only on the universal scaling function f_s and a universal exponent ζ. One speaks of a fixed point of the renormalisation group flow when a change of scale s no longer affects the correlator C. In this case the scaling functions become a power law characterised only by the universal exponent.

In recent years, the renormalisation group approach has been extended to systems far from equilibrium by using time t as the flow parameter instead of the spatial resolution s. It has been proposed that a system on its way to equilibrium may pass through a regime, where correlation functions rescale in the same way as before. The only difference is that the scaling function now depend on two separate scaling exponents α and β: $C(t, k) = (\frac{t}{t_{\mathrm{ref}}})^{\alpha} f_s((\frac{t}{t_{\mathrm{ref}}})^{\beta} k)$, where t_{ref} is a reference time within the scaling regime. The fixed point associated with this so-called dynamical scaling hypothesis is called the non-thermal fixed point. Also, at the non-thermal fixed point, the correlator takes its characteristic power-law form, which is directly related to a critical slowing down (or speeding up) of the time evolution, depending on the sign of β. The whole concept is visualised on the left in Fig. 2.4. Note that we have used the momentum correlator, which behaves identically to its spatial counterpart and is commonly used in other work. This thesis is mainly concerned with the occupation number in momentum space and we want to use the rest of this section to discuss its form. As shown on the right in Fig. 2.4 $f(t, k)$ has different scaling exponents depending on the regime under consideration. While the typically negative value of β in the ultraviolet (UV) is associated with energy transport to a few fast particles, in the infrared (IR) one generally observes positive β, indicating a slowing down of the particles. By using appropriate conservation laws one can find relations between α and β. For example, if the conservation of particle numbers is respected, which is classically the case in the IR, then the quantity

$$\int d^d k f(t, k) \tag{2.22}$$

is conserved and one finds the relation $\alpha = d\beta$. In this thesis we are mainly interested in the IR part of the spectrum, which typically consists of a plateau and then falls

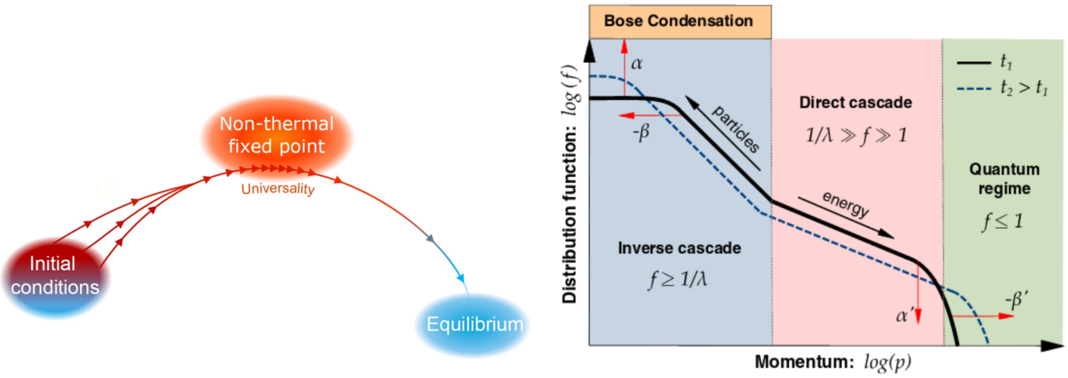

Figure 2.4: Left: A schematic representation of a non-thermal fixed point is shown. This fixed point is characterised by the dynamics of a system placed in a far from equilibrium initial state. The system evolves universally upon reaching the fixed point. Figure taken from [23]. Right: A schematic illustration of the occupation number distribution near a non-thermal fixed point, plotted as a function of momentum for two consecutive times, t_1 and t_2. The self-similar evolution is characterised by the scaling exponents α and β, as described in Equation 2.4. Figure taken from [24].

off with a characteristic power law k^{κ}. In the course of this work we want to extract the values for α, β and κ in polariton condensates and relate them to the underlying KPZ universality class.

2.5 Transition to the Kardar-Parisi-Zhang equation

The aim of this section is to formalise the connection between the Kardar-Parisi-Zhang universality and the polariton model. This has already been done by [21], which we follow closely here. We start with the generalised GPE describing the polariton condensate:

$$\begin{aligned} i\frac{\partial}{\partial_t}\Psi(x,t) =& \Big[-\frac{\Delta}{2m} - i\frac{\gamma_2}{2}\Delta + \frac{i}{2}(Rn_R - \gamma_0) + g|\Psi(x,t)|^2 + 2g_R n_R \Big] \Psi(x,t) \\ &+ \xi(x,t) \qquad (2.23) \\ \frac{\partial}{\partial_t} n_R(x,t) =& P - (\gamma_R + R|\Psi(x,t)|^2) n_R(x,t). \qquad (2.24) \end{aligned}$$

We choose a hydrodynamic ansatz for the condensate wave function in a rotating frame

$$\psi(x,t) = \sqrt{\rho(x,t)}\exp i(\theta(x,t) - \omega_o t). \tag{2.25}$$

The polariton and reservoir densities are subject to a restoring force that relaxes them to their stationary values within a short time. It is therefore convenient to describe the densities as fluctuations around a stationary mean field value. Provided that these fluctuations are small and stationary, i.e.

$$\delta\rho = \rho(x,t) - \rho_0 \qquad \delta\rho/\rho_0 \ll 1 \tag{2.26}$$

$$\delta n_R = n_R(x,t) - n_{R,0} \qquad \delta n_R/n_{R,0} \ll 1 \tag{2.27}$$

$$\partial_t\delta\rho = \partial_t\delta n_R = 0 \tag{2.28}$$

Eq. 2.24 can be rewritten as:

$$Rn_R = \frac{P}{\frac{\gamma_R}{R} + \rho}. \tag{2.29}$$

We first focus on the mean field by inserting the stationary phase rotation $\psi = \sqrt{\rho_0}e^{-i\omega_0 t}$ into Eq. 2.23. Separating real and imaginary part leaves us with two equations:

$$\gamma_0 = Rn_{R,0} = \frac{P}{\frac{\gamma_R}{R} + \rho_0} \tag{2.30}$$

$$\omega_0 = 2g_R n_{R,0} + g\rho_0 = \frac{g_R\gamma_0}{R}\Big[2 + \frac{g}{g_R}\frac{\gamma_R}{\gamma_0}(\frac{PR}{\gamma_R\gamma_0} - 1)\Big]. \tag{2.31}$$

The first line describes the magnitude of the mean densities, while the second line gives us a formula for the condensate emission frequency. To go beyond the mean-field level, we first examine the derivatives of the wave function within our approximation. We also neglect terms containing spatial derivatives of the condensate density:

$$\partial_t\psi = \psi(\rho^{-1}\partial_t\rho + i\partial_t\theta - i\omega_0) \approx \psi(i\partial_t\theta - i\omega_0) \tag{2.32}$$

$$\begin{aligned}\partial_x^2\psi =& \psi(\frac{1}{2}\rho^{-1}\partial_x^2\rho - \frac{1}{4}\rho^{-2}(\partial_x\rho)^2 - (\partial_x\theta)^2 + i\rho^{-1}\partial_x\rho\cdot\partial_x\theta + i\partial_x^2\theta)\\ &\approx \psi(-(\partial_x\theta)^2 + i\partial_x^2\theta).\end{aligned} \tag{2.33}$$

Inserting these expressions for the derivatives into Eq. 2.23 we end up with:

$$
\begin{aligned}
\partial_t\theta =& -\omega_0 - \frac{1}{2m}(\partial_x\theta)^2 - 2g_R n_R - g\rho + \Re\{\bar{\xi}\} && (2.34)\\
0 =& \frac{1}{2m}\partial_x^2\theta + \frac{1}{2}(Rn_R - \gamma_l) + \Im\{\bar{\xi}\} && (2.35)\\
P =& Rn_R(\frac{\gamma_R}{R} + \rho). && (2.36)
\end{aligned}
$$

Now we can use the two equations from our mean field considerations to simplify the model equations. Writing everything in terms of fluctuations, we obtain the three equations:

$$
\begin{aligned}
\partial_t\theta =& -\frac{1}{2m}(\nabla\theta)^2 + \frac{\gamma_2}{2}\nabla^2\theta - g\delta\rho - 2g_R\delta n_R + \Re\{\bar{\xi}\} && (2.37)\\
\delta n_R =& \frac{2}{R}\left[\frac{1}{2m}\nabla^2\theta + \frac{\gamma_2}{2}(\nabla\theta)^2 - \Im\{\bar{\xi}\}\right] && (2.38)\\
\delta\rho =& -\frac{PR}{\gamma_0^2}\delta n_R. && (2.39)
\end{aligned}
$$

The three equations above can be combined into one formula by a simple substitution. The resulting equation describes the effective evolution of the phase and has the form of the Kardar-Parisi-Zhang equation [25]:

$$
\begin{aligned}
\partial_t\theta =& \Big[\frac{\gamma_2}{2} - \frac{2g_R}{Rm} + \frac{Pg}{m\gamma_0^2}\Big]\partial_x^2\theta - \Big[\frac{1}{2m} + \frac{2g_R\gamma_2}{R} - \frac{Pg\gamma_2}{\gamma_0^2}\Big](\partial_x\theta)^2 + \eta && (2.40)\\
\equiv& \nu\nabla^2\theta + \frac{\lambda}{2}(\nabla\theta)^2 + \eta && (2.41)
\end{aligned}
$$

with

$$
\begin{aligned}
\langle\eta(x,t)\eta(x',t')\rangle =& \frac{\xi_0}{\rho_0}\left[1 + 4\left(2\frac{g_R}{R} - \frac{Pg}{\gamma_0^2}\right)^2\right]\delta(x-x')\,\delta(t-t') && (2.42)\\
\equiv& \, 2D\delta(x-x')\,\delta(t-t')\,. && (2.43)
\end{aligned}
$$

It is worth taking a closer look at the coefficients of the KPZ equation. For the linear limit of the KPZ equation, i.e. the Edwards-Wilkinson equation, to be stable, the effective diffusivity ν must be positive. In our simulations we assumed that the reservoir-induced blueshift $2g_R n_R$ dominates over the polariton-polariton interactions, thus setting the interaction strength g to 0. In this case a sufficiently large linewidth γ_2 is crucial for stable phase dynamics.

3 Numerical Methods

The generalised Gross-Pitaevskii equation presented in section 2.3 serves as the foundation for investigating the condensation of polariton-exciton systems. Unfortunately, this equation is a coupled, non-linear equation which proves too complicated for analytical solutions. Consequently, we must rely on the power of numerical computation to explore this phenomenon. All numerical simulations in this thesis were performed using a self-written Python code that takes advantage of the powerful GPU-accelerated numerical computing capabilities provided by CUDA. CUDA, a parallel computing platform and API, enables the utilisation of graphical processing units (GPU) for general purpose computing. To access these capabilities, we employed the CuPy Python library, which seamlessly integrates with CUDA allowing for high performance numerical computations. Much of the efficiency of the code comes from this GPU acceleration, particularly when executing discrete fast Fourier transforms or handling large matrix operations. Our code draws significant inspiration from a previous C++ code developed in the research group of Prof. Dr. Thomas Gasenzer and originally used to investigate the dynamics of BECs far-from equilibrium [26, 27]. In particular, the idea of employing the split-step Fourier algorithm to solve the generalised Gross-Pitaevskii equation, as well as the utilization of the semi-classical truncated Wigner approximation (TWA) for calculations beyond the mean-field configuration, originated from that code.

This chapter serves as an introduction to the relevant numerical concepts - the simulation results obtained are discussed in the next chapter. We start with the discretisation of wave functions on a lattice and the convergence between numerical and physical units. We then outline the workhorse of our simulation, the split-step Fourier algorithm, which is used to obtain the time evolution of the system. The fundamental idea behind this algorithm is to employ a series of alternating steps, utilizing fast Fourier transforms and direct diagonalisations, to efficiently and accurately solve the time-dependent Gross-Pitaevskii equation. By leveraging the diagonal nature of the momentum space part, the algorithm becomes computationally more tractable and well-suited for numerical simulations.

The final chapter is concerned with the truncated Wigner approximation, a semi-classical technique that goes beyond mean-field theory to include quantum effects. The TWA approximates the field through its classical c-number representation and evolves it using the Gross-Pitaevskii equation. Fluctuations are introduced in its initial momentum state, according to the Wigner distribution. By accumulating and averaging many individual trajectories, this method effectively captures the dynamics with lowest order quantum fluctuations.

3.1 Converting to numerical units

We begin by outlining the essential steps involved in discretising the wave functions on a spatial grid. This discretisation enables the conversion of continuous equations of motion into a discrete form that can be solved numerically. The first step is to specify a suitable spatial grid. In this work we use a one-dimensional grid, typically consisting of $n_g = 8192$ grid points.

The lattice spacing, denoted by a_g, establishes a length scale. This scale is used to assign numerical values to the physical parameters of the system. In this regard, we also set both Planck's constant, $\hbar = 1.05 \cdot 10^{-34} \frac{m^2 kg}{s} = 1$, and the lattice spacing, $a_g = \frac{L}{n_g} = 1$, to unity, where L is the physical length of the system. Additionally we define the mass of the polaritons to be $m_p = \frac{1}{2}$. Once these conditions are in place, it is possible to calculate the numerical values of all physical parameters. For example, all times would simply be rescaled with the factor $T_{\text{scale}} = \frac{a_g^2 m_p}{\hbar}$.

In the following chapters, the numerical values of a given simulation are stated explicitly. To determine the momentum grid corresponding to a given spatial grid, it is necessary to perform a Fourier transformation. The lattice momenta are derived by expanding the fields in discretised plane waves and inserting them into the discrete Laplacian

$$\frac{\partial^2}{\partial x^2}\Psi = \frac{\Psi(x_{j+1}) + 2\Psi(x_j) + \Psi(x_{j-1})}{a_g^2}. \tag{3.1}$$

This results in the following relation for the lattice momenta:

$$k_n = \frac{2}{a_g} \sin \frac{\pi n}{n_g} \tag{3.2}$$

with $n \in [-\frac{n_g}{2}+1, \frac{n_g}{2}]$. Therefore, the maximum lattice momentum is $k_{\max} = \frac{2}{a_g}$. The main reason behind this definition is the congruence between the split-step Fourier method and finite difference methods in the treatment of partial differential equations. The choice of the discrete Laplacian, and hence sinusoidal rather than linearly spaced momenta, leads to inhomogeneities in the spectrum. In particular, the spacing in the ultraviolet (UV) is denser than the almost linear spacing in the infrared (IR). It is therefore useful to regulate the resolution of the simulation by adjusting the UV and IR cut-offs of the momentum grid.

3.2 Split-Step Fourier

As mentioned in the introduction to this chapter, the split-step Fourier algorithm is our preferred method for performing the time integration of the Gross-Pitaevskii-type equation. This algorithm offers significant advantages, as it conserves both the total number of particle and the total energy of the system. Additionally, it seamlessly aligns with the utilization of GPU-accelerated computation, increasing computational efficiency.

At its core, the split-step Fourier algorithm operates by effectively splitting the Hamiltonian into two distinct parts: one that is diagonal in momentum space, denoted as $\mathcal{D}$, and another containing all remaining terms, denoted as $\mathcal{N}$. This separation is achieved by isolating all terms that involve second-order derivatives

$$i\partial_t \psi(x,t) = H\psi(x,t) \Rightarrow \quad \psi(x,t+\Delta t) = e^{-i\Delta t H}\psi(x,t) = e^{-i\Delta t(\mathcal{D}+\mathcal{N})}\psi(x,t). \tag{3.3}$$

If the simultaneous diagonalisation of $\mathcal{D}$ and $\mathcal{N}$ were possible, calculating the time-evolution would be straightforward. However, this is generally not the case. Instead, we employ the Baker-Campbell-Hausdorff formula to split the exponential function into two separate operations, incurring an error of order $\mathcal{O}(\Delta t^2)$. By using this approach, the kinetic part $\mathcal{D}$ becomes easily solvable in Fourier space, while $\mathcal{N}$ is still a simple multiplication in real space. Therefore, the overall expression computed by the algorithm at each time step contains a Fourier transform and can be expressed as follows:

$$\psi(x,t+\Delta t) = e^{-i\Delta t\mathcal{N}}\mathcal{F}^{-1}\{e^{-i\Delta t\mathcal{D}}\mathcal{F}(\psi(x,t))\}\} + \mathcal{O}(\Delta t^2). \tag{3.4}$$

This expression, consisting solely of diagonal multiplications within their respective spaces, can be efficiently vectorised and reduced to a straightforward multiplication at each grid point. This task aligns well with the capabilities of a GPU, making it highly suited for parallel computation. Together with the implementation of the Fast Fourier Transform routine, this contributes significantly to the performance of the code.
In our code a three fractional step is used to further enhance accuracy. As a result, we achieve the final integration scheme for one time step as follows:

$$\psi(x,t+\Delta t) = \mathcal{F}^{-1}\{e^{-i\frac{\Delta t}{2}\mathcal{D}}\mathcal{F}[e^{-i\Delta t\mathcal{N}}\mathcal{F}^{-1}\{e^{-i\frac{\Delta t}{2}\mathcal{D}}\mathcal{F}(\psi(x,t))\}]\} + \mathcal{O}(\Delta t^3). \tag{3.5}$$

For the generalised GPE of a polariton-exciton condensate considered in this thesis, the splitting of the Hamiltonian leads to the two parts:

$$\mathcal{D} = \frac{k^2}{2m} - \frac{i\gamma_2 k^2}{2} \tag{3.6}$$

$$\mathcal{N} = \frac{i}{2}(Rn_R - \gamma_0) + g|\Psi(x,t)|^2 + 2g_R n_R. \tag{3.7}$$

The noise can be added either in momentum or real space, in our implementation we chose to add ξ in momentum space. The coupled equation governing the exciton reservoir is in many ways much easier to solve, as it does not contain spatial derivatives. Here we use a simple Euler step to calculate its time evolution:

$$n_R(x,t+\Delta t) = n_R(x,t) + \Delta t[P - (\gamma_R + R|\Psi(x,t)|^2)n_R(x,t)]. \tag{3.8}$$

3.3 Truncated Wigner Approximation

While the classical approach to BEC has demonstrated its merit, there are instances where a departure from the mean-field perspective is necessary. This becomes especially relevant when focusing on modes with low occupancy, diverging from the classical solution provided by the Gross-Pitaevskii equation. Such deviations arise, for example, in driven-dissipative Bose gases with multi-stable states or in the dynamic filling processes of interconnected condensates. In these complex scenarios, a more comprehensive understanding is required, leading to the inclusion of quantum fluctuations. As the polariton-exciton condensate is governed by a coupled equation with complex filling dynamics, it falls into the realm of systems where traditional mean-field approximations prove insufficient.

In our numerical simulations we implemented the truncated Wigner approximation (TWA), to circumvent this problem. The TWA, a semi-classical technique well-established in quantum optics, bridges the gap between classical and quantum descriptions. The fundamental idea behind the TWA is to sample initial conditions from the Wigner distribution and evolve these quasi-classical trajectories using classical equations of motion. Evolving over many of these individual trajectories and averaging them at the end recovers the dynamics, including the lowest order quantum fluctuations.

While this method incorporates some quantum effects, such as interference, it neglects the full quantum correlations that may be present in the true quantum evolution. As with all when it comes to computational simulations, there is a trade-off between computational feasibility and capturing key quantum features. Below is a more detailed description of the TWA following [28],[29].

We start by defining the Weyl transformation of an arbitrary operator $\hat{A}(\Psi, \Psi^\dagger)$ as:

$$A_W(\Psi, \Psi^\dagger) = \int\int \frac{d\alpha^* d\alpha}{2^D} \langle \Psi - \frac{\alpha}{2} |\, \hat{A}(\Psi, \Psi^\dagger) \,| \Psi + \frac{\alpha}{2} \rangle \, e^{-|\Psi|^2 - \frac{1}{4}|\alpha|^2} e^{\frac{1}{2}(\alpha^* \Psi - \alpha \Psi^*)}. \tag{3.9}$$

Next we define the Wigner function as the Weyl transformation of the density matrix $\hat{\rho}$ of a quantum state:

$$\mathcal{W}(\Psi, \Psi^\dagger) = \hat{\rho}_W = \int\int \frac{d\alpha^* d\alpha}{2^D} \langle \Psi - \frac{\alpha}{2} |\, \hat{\rho}(\Psi, \Psi^\dagger) \,| \Psi + \frac{\alpha}{2} \rangle \, e^{-|\Psi|^2 - \frac{1}{4}|\alpha|^2} e^{\frac{1}{2}(\alpha^* \Psi - \alpha \Psi^*)}. \tag{3.10}$$

The Wigner function acts as a quasi-probability distribution, allowing for negative values unlike classical probability functions. For large occupation numbers the Wigner function is semi-positive definite, enabling it to function as a classical probability distribution function [30]. By inserting the density matrix in Equation 3.9, it is possible to demonstrate that the expectation value of any operator is given by an average over the Wigner distribution:

$$\langle \hat{A}(\Psi, \Psi^\dagger) \rangle = \int\int d\Psi d\Psi^* \mathcal{W}(\Psi, \Psi^\dagger) A_W(\Psi, \Psi^\dagger). \tag{3.11}$$

The goal is to Weyl transform the von Neumann equation, as it characterises the quantum dynamics of a density matrix in the Schrödinger picture:

$$i\hbar\frac{\partial\hat{\rho}}{\partial t} = [\hat{H}, \hat{\rho}]. \tag{3.12}$$

The transformation of the left-hand side is straightforward, as it can be easily simplified into the time-derivative of the Wigner function. The right-hand side, on the other hand, requires a more complicated treatment. Therefore, we first look at Weyl transformations of operator products, where we find a Moyal product relation [31]:

$$(A_1 A_2)_W = A_{1,W} \exp\frac{\Lambda}{2} A_{2,W} \tag{3.13}$$

where Λ is the symplectic coherent state operator:

$$\Lambda = \sum_j \overleftarrow{\frac{\partial}{\partial\Psi_j}\frac{\partial}{\partial\Psi_j^*}} - \overrightarrow{\frac{\partial}{\partial\Psi_j}\frac{\partial}{\partial\Psi_j^*}}. \tag{3.14}$$

The arrows in the above definition indicate the direction on which the differential operators operate. With the help of Equation 3.13 we can express the Weyl transformation of a commutator as

$$([A_1, A_2])_W = 2A_{1,W} \sinh\frac{\Lambda}{2} A_{2,W} \tag{3.15}$$

and finally find that the Weyl transformation of the von Neumann equation is given by:

$$i\hbar\frac{\partial\mathcal{W}}{\partial t} = 2H_W \sinh\frac{\Lambda}{2}\mathcal{W}. \tag{3.16}$$

In order to solve the equation of motion, we expand the hyperbolic sine in Λ and truncate it in leading order. This is justified in the case of high occupation numbers, because Λ scales roughly with the inverse modulus squared of the wave function. At high occupation numbers this becomes a very large number and the leading orders of the series expansion dominate, while higher order terms become less and less significant. This truncation is called the truncated Wigner approximation, which leaves us with the classical Liouville equation, where $\{,\}_P$ denotes the Poisson bracket

$$i\hbar\frac{\partial\mathcal{W}}{\partial t} = \{H_W, \mathcal{W}\}_P. \tag{3.17}$$

The solution of the Liouville equation may be obtained, for example, by using the method of characteristics [32]. We find that the classical GPEs are indeed the solutions, even in the semi-classical case

$$i\hbar\frac{\partial\Psi}{\partial t} = \frac{\partial H_W}{\partial\Psi^*}. \tag{3.18}$$

The differences to an entirely classical description stem from the fact that we used expectation values when defining Eq. 3.11, rather than using the operators directly. Consequently, we have to average over many realisations to extract the desired expectation value of an observable. However, the time evolution is still governed by the classical GPE. So rather than evolving the Wigner function itself in time, we sample a large number of initial conditions chosen randomly according to the weight of the Wigner function. In the case of a coherent state, the initial Wigner function is simply given by a Gaussian, with an average occupation of half a particle in each mode. Note that this implies that the vacuum state has a virtual occupation of half a particle, which can only be subtracted after averaging.

4 Simulation Results

In this chapter we present the results obtained through numerical integration of equations 2.21, which govern the time evolution of a polariton-exciton condensate. To achieve this, the techniques described in the previous chapter have been employed, in particular the usage of the split-step Fourier algorithm for time integration and the truncated Wigner approximation to account for quantum effects within the simulation.

The organisation of the chapter is divided into two primary sections, each corresponding to a different parameter regime that we have examined through simulations. The first regime attempts to replicate the condensate studied in the work of Fontaine et al. [21], which established the connection between one-dimensional polariton-exciton condensates and the KPZ equation, as well as the emergence of space-time vortices. This particular regime is of special interest because similar vortex structures in the time-space domain have been observed in the context of one-dimensional spin-1 Bose-Einstein condensates, a phenomenon observed by Prof. Gasenzer's research group [33].

The other parameter regime, which is only weakly based on an experimental realisation, revolves around the concept of self-similar scaling. Although this regime exhibits structures that manifest within the space-time plane of density and phase, they are not as pronounced as those in the first regime. Instead, this particular regime exhibits a pattern of self-similar scaling within the momentum occupation number. This is particularly interesting in the context of identifying non-thermal fixed points in the dynamics of systems far from equilibrium - a class of systems into which the polariton condensate may fall.

Both of these subsections are structured in a somewhat analogous manner. We begin by specifying the parameter regime through stating the numerical values of all physical parameters. Subsequently, we provide a visual representation illustrating the density and phase of a singular simulation run. Finally, we present the results of further investigation within the given regime. The subsequent section begins with an exploration of the first parameter regime, where the presence of space-time vortices is a prominent feature.

4.1 Regime of space-time vortices

As mentioned in the introductory section of this chapter, the motivation for this study originates from a recent publication in the journal Nature [21]. The central aim of this publication was to explore the connection between the KPZ equation and one-dimensional exciton-polariton condensates. However, it was the appearance of space-time vortices that inspired this thesis. In particular, the striking visual similarity between these vortices and a separate class of space-time vortices discovered in simulations of a spin-1 Bose-Einstein condensate by the Gasenzer research group. For comparison, Figure 4.1 shows simulation instances from both systems, providing a visual representation of the resulting vortices. In both systems we observe the presence of lines with a constant phase value propagating through time. At the location of a vortex, the phase undergoes a complete 2π wrapping around a central point. The direction of this phase wrap determines whether it is a vortex or an antivortex. Interestingly, in the polariton system of [21], the dynamics show the appearance of vortex-antivortex pairs, maintaining the total winding number of the

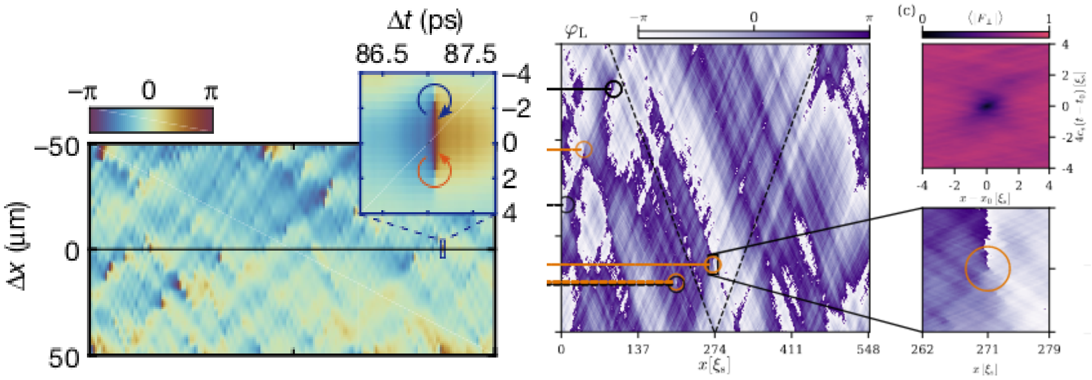

Figure 4.1: Space-time vortices in two different physical systems: On the left, a simulation illustrating the phase evolution of a one-dimensional polariton-exciton condensate [21]. Colour coding represents phase values ranging from $-\pi$ to π. The inset provides a detailed view of a vortex-antivortex pair. On the right, a simulation showing the Larmor phase of the transverse spin, orientated in the F_x-F_y plane, in a one-dimensional spin-1 BEC, as featured in [33]. Close-up views reveal an emerging vortex, evident both as a dip in transverse spin density and as phase wrapping around a central point in the Larmor phase.

system, whereas in the spin-1 case, single vortices appear.
We began our investigation with the simulation of the polariton condensate described in [21]. Despite employing the exact parameters described in [9], our results exhibited significant disparities. The source of this discrepancy remains unclear, with no obvious explanation. The only difference in approach lies in the different integration methods used. While our approach focused on the use of the split-step Fourier algorithm, the cited work relied on the semi-implicit Runge-Kutta method for temporal integration. The numerical values characterising this particular regime are given below for reference.

$$\begin{array}{ccc}
m_p = -3.3 \cdot 10^{-6} \cdot m_e = -3.01 \cdot 10^{-36} & a_g = 4.4 \cdot 10^{-7} & T_{\text{Scale}} = 1.10 \cdot 10^{-14} \\
\gamma_0 = 8.13 \cdot 10^{-4} & \gamma_2 = 1.39 & \gamma_r = 3.66 \cdot 10^{-4} \\
g_R = 1.36 \cdot 10^{-4} & R = 2.21 \cdot 10^{-5} & P = 1.49 \cdot 10^{-2}
\end{array}$$

Table 4.1: Numerical values of physical parameters used in [9] to simulate exciton-polariton condensates with space-time vortices

The table above does not specify the value of the polariton-polariton interaction strength g. We have adopted the reasoning presented in [9], where it was argued that the reservoir-induced blueshift $2g_R n_R$ significantly outweighs the interaction strength. Consequently, we set g to zero. Examining Eq. 2.41, which describes the mapping of the KPZ equation to the polariton system, a vanishing g introduces certain constraints on the system. In particular, the first coefficient of the KPZ equation, denoted ν, must be positive to ensure stable KPZ dynamics. This condition holds only if the momentum dependent loss rate γ_2 is sufficiently large or if the polariton mass is tuned to negative values. In line with the approach of [9], we have chosen to assign negative values to our polaritons to avoid this problem.
The specific choice between periodic and static boundary conditions did not affect the simulation, in the following we use periodic boundary conditions. In contrast, we observed that modifying the pumping profile had a significant influence on the behaviour of the condensate in our simulations. Following the recommendation in [9], we used a spatially varying flat-top pump profile in all our simulations. This profile is defined by the equation presented below and visually illustrated in Fig. 4.2:

$$P(x) = P\frac{[1+\tanh(\frac{L_0+x}{\sigma})][1+\tanh(\frac{L_0-x}{\sigma})]}{[1+\tanh(\frac{L_0}{\sigma})]^2} \tag{4.1}$$

Here $L_0 = 80\mu m$ represents the length of the pump spot and $\sigma = 9.7\mu m$ characterises the width of its decaying edges. With these original parameter values the condensate was unstable and collapsed after short times. Remarkably, it was possible to obtain a stable condensate by only scaling both the overall system size and the values of L_0 and σ by a factor of 10. As a result, the updated parameters ($L_0 = 800\mu m$ and $\sigma = 97\mu m$) were used in subsequent simulations. To account for the increased system size, the simulation was run on an enlarged lattice of 4096 lattice sites, keeping the lattice spacing a_g constant. The results of this simulation with the updated parameters are shown in Fig. 4.3. The profound impact of the pumping profile on the behaviour of the condensate is immediately apparent. The condensate closely mimics the shape of the pumping profile, resembling a roughly rectangular structure with minimal density at the edges. This correspondence between the shape of the condensate and the profile of the pumping beam is not surprising, as the pumping beam effectively imprints its shape on the exciton reservoir and subsequently influences the form of the condensate.

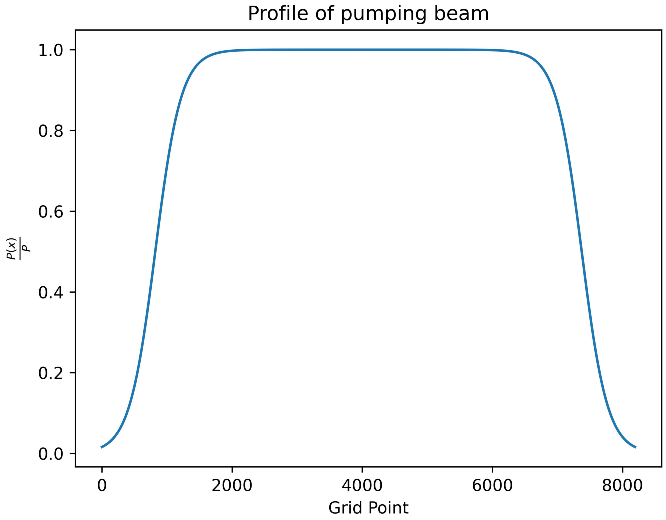

Figure 4.2: Visual representation of the pumping profile defined in 4.1 used to stimulate the exciton reservoir. The shape is imprinted through interaction on the condensate.

Furthermore, our simulation reveals the emergence of defects in both density and phase evolution. These defects are characterised by local density dips in the condensate, which appear as dark lines in the density evolution plots. They are slightly less prominent in the phase evolution, where they indicate a phase jump and appear

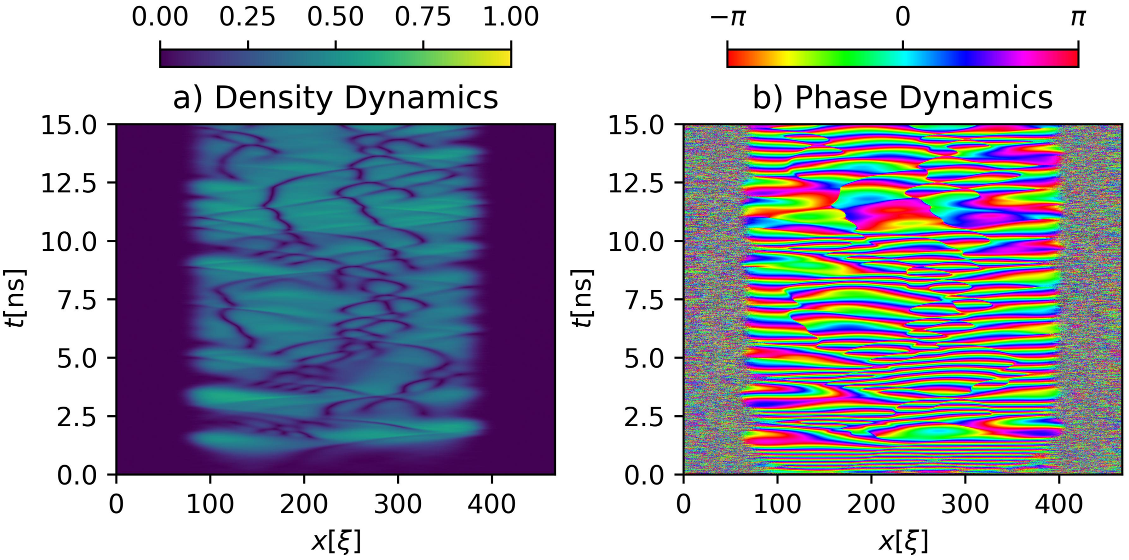

Figure 4.3: Simulation depicting the time evolution of a polariton condensate with pump parameters $L_0 = 800\mu m$ and $\sigma = 97\mu m$, evolving over a maximum propagation time of 15 ns in real space. In the spatial direction, given in units of healing length, the simulation extends over 4096 grid points: a) Illustrates the evolving condensate density, with clearly visible dark lines representing defects propagating within the condensate. b) Displays the time evolution of the condensate phase, where defects manifest as visible lines separating regions characterized by constant phase values.

as lines separating regions of constant phase values. To gain a clearer perspective on these emerging structures within the polariton dynamics, we have zoomed in and increased the temporal resolution. Figure 4.4 shows a simulation run with the same parameters as before, but allows a closer examination by focusing on the time interval from 13 ns to 14 ns. The close-up view allows us to examine the emerging defects within the condensate in detail. In particular, we observe a direct alignment between the dark lines in the density plot and the phase jumps in the phase dynamics plot. This alignment supports the hypothesis that these propagating defects are dark solitons. Dark solitons are characterised not only by local dips in condensate density but also by accompanying phase jumps. To validate this hypothesis, we performed a more detailed analysis of the defects. In particular, we wanted to check whether the density profile of these defects is consistent with the expected

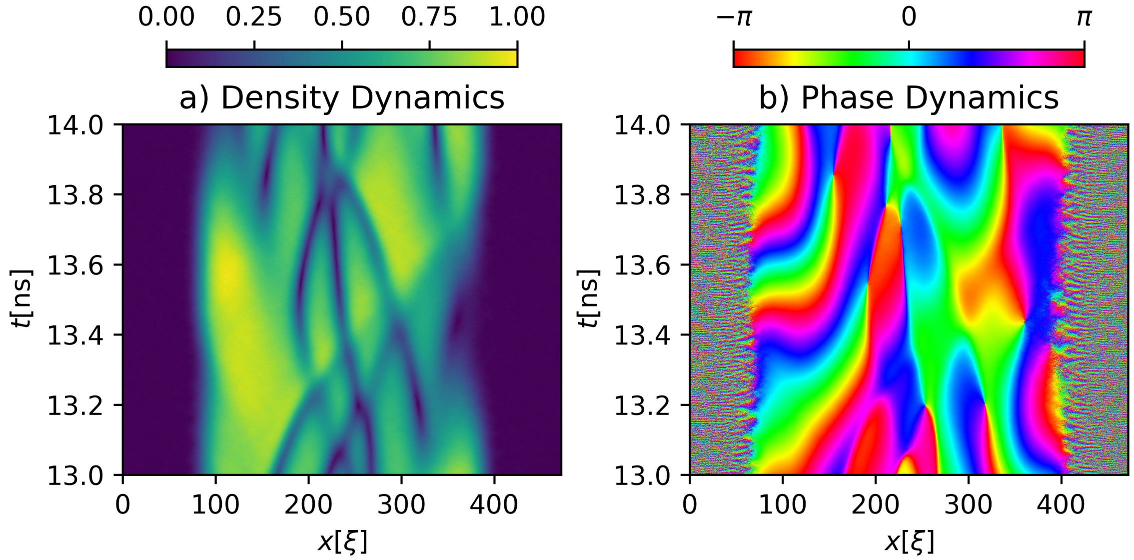

Figure 4.4: This Figure provides a more detailed temporal view of the simulation shown in Figure 4.3. The evolution of the condensate is shown over the time interval from 13 ns to 14 ns, highlighting the emergence of structures. a) highlights the defects in the density of the condensate, while b) shows the defects in the phase dynamics. Notably, the alignment between density and phase defects suggests soliton-like behaviour. Furthermore, in the phase plot (b), intersections of these defects, where multiple phase jumps occur, are distinguished as cores of vortex-like structures within the condensate (see e.g. two vortex cores at 13.2 ns).

dark soliton pattern described by the formula:

$$\rho(x) = \rho_0 \Big| \frac{1}{\gamma} \tanh\left[\frac{1}{\sqrt{2}\gamma\xi}(x - x_{\text{mean}})\right] + i\sqrt{1 - \frac{1}{\gamma^2}} \Big|^2 \tag{4.2}$$

Here ρ_0 is the mean density of the condensate, ξ denotes its healing length and $\gamma = (1 - (\frac{v}{c_s})^2)^{-\frac{1}{2}}$ represents the Lorentz factor associated with the speed of sound. Figure 4.5 a) illustrates the fitting of this function to a density dip. The fit closely matches the actual density profile of the defect, with slight discrepancies at the edges due to the presence of multiple defects.

To further confirm that these defects are, indeed, dark solitons, we need to demonstrate that the phase exhibit jumps at their positions. Although there is some direct evidence for phase jumps in the phase evolution plot, we conduct a more detailed examination by introducing a quantity called 'solitonicity'. This measure is defined as:

$$S(t, x) = |\rho_0 - \rho(t, x)||\partial_x \theta(t, x)| \tag{4.3}$$

In essence, this observable only reacts when both a density dip and a phase jump coexist at the same location. The solitonicity for our simulation run is depicted in Figure 4.5 b). We can see that, apart from the edges, the positions of the defects align with regions of high solitonicity. This alignment allows us to classify these defects as dark solitons, and we will refer to them as such from this point onwards. The solitonicity measure is most pronounced at the points where dark solitons intersect. When we revisit the phase dynamics plot in Figure 4.4, these points become distinct as the cores of vortex-like structures, characterised by multiple phase jumps occurring at these intersections. We refer to these phenomena as 'space-time vortices', when the phase undergoes a complete 2π change as one encircles the central point. An example of such a vortex can be seen in Figure 4.6, where we have

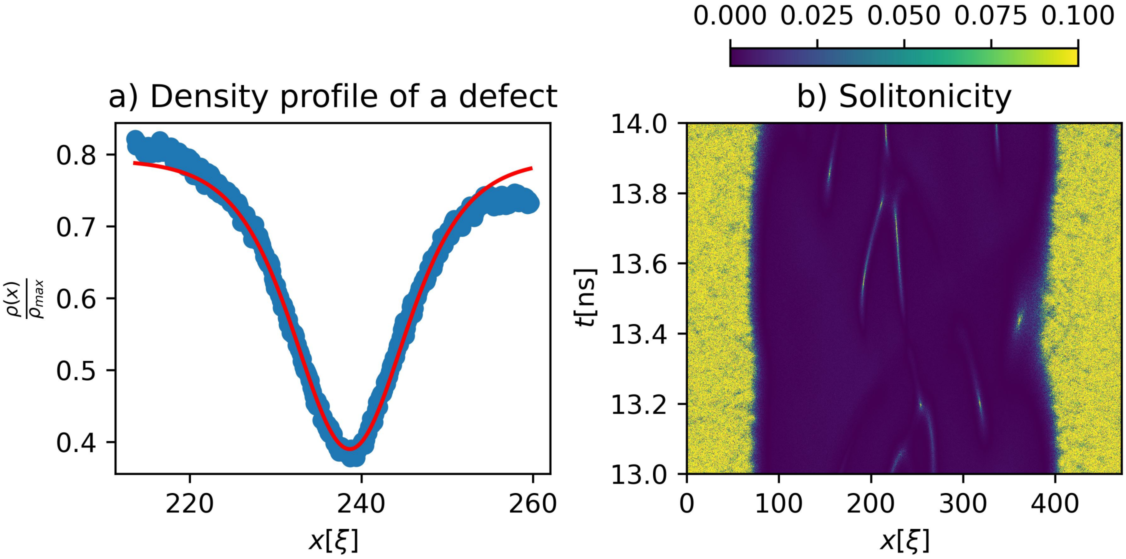

Figure 4.5: Analysis of emerging defects in condensate dynamics: a) Demonstrates the fitting of the typical density profile of a dark soliton, as described in Equation 4.2, to the density dip associated with a defect. The small discrepancies observed at the edges are attributed to the presence of multiple defects. b) Presents a plot of solitonicity $S(t, x) = |\rho_0 - \rho(t, x)||\partial_x \theta(t, x)|$, an observable that measures the simultaneous occurrence of a phase jump and a density dip. This plot closely matches the defects shown in Figure 4.4, providing strong evidence to classify these defects as dark solitons.

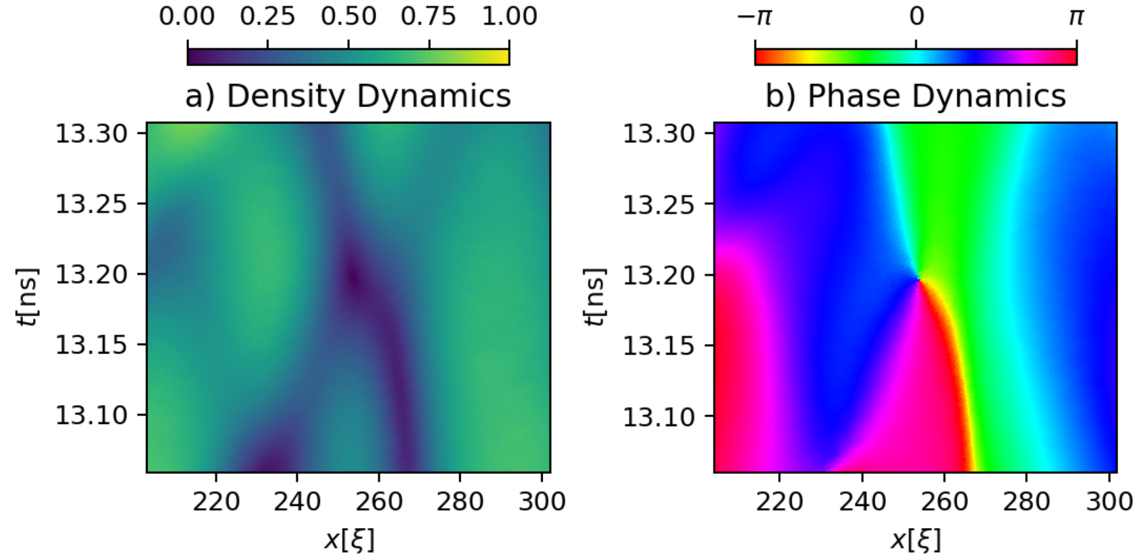

Figure 4.6: Close-up of a space-time vortex from Fig. 4.4: This image provides a detailed view of the intersection of two dark solitons. Notably, the core of the space-time vortex aligns exactly with this intersection point, where the condensate density reaches its minimum value. The space-time vortex is characterised by a continuous traverse of the colour scale used to represent the phase, indicating a phase change of 2π.

zoomed in on one such crossing point. In this figure, the vortex is characterised by its continuous traversal of the colour scale used to represent the phase. At the same time, the density plot shows the intersection of two solitons. The core of the vortex coincides exactly with the intersection point where the density reaches its minimum value. Taken together, these observations provide compelling evidence to classify this pattern as a space-time vortex. Consequently, we can confirm that this particular parameter regime does indeed lead to the formation of such vortices.

Unfortunately, in this specific parameter regime, we do not observe an approach to a so-called non-thermal fixed point. In order to investigate whether a regime of universal scaling is imminent, we analysed the occupation number in momentum space at different points in time. The results of this investigation are shown in Figure 4.7. In particular, we observe that, with the exception of a few early times, all occupancy spectra coincide. This is in contrast to expectations in the vicinity of a non-thermal fixed point, where self-similar scaling should occur, as we will show in the following section.

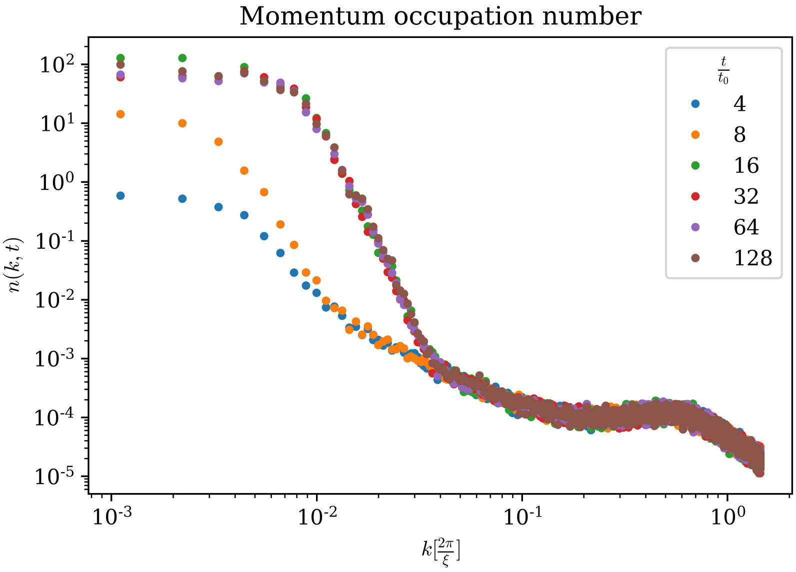

Figure 4.7: The momentum occupation spectrum is obtained by plotting the occupation number in momentum space at different time points. The last time point at 128 corresponds to 15 ns. This plot is generated by averaging the results of 50 simulation runs. It is noticeable that the spectra overlap at late times, suggesting that there is no scaling behaviour in the system. System parameters are listed in table 4.1 at the start of the section, most importantly $g = 0$.

4.2 Regime of self-similar scaling

This section is devoted to a specific parameter regime which has been found to exhibit both a distinct structure in the evolution of the density and a self-similar scaling pattern in the momentum occupation. The inspiration for this regime can be partly traced back to the parameters used in the Grenoble experiments [34, 35], albeit with a significantly different approach. Whereas they considered a system in which polariton-polariton interactions dominate over polariton-exciton interactions, our focus in this investigation has been reversed. Therefore, we set $g = 0$ and neglected the polariton-polariton interaction completely. The reader is referred to [36] for further reading on numerical simulations of the Grenoble experiments. In order to define this focus, the numerical values of the parameters used in the simulation of this section are listed in the following table.

$$\begin{array}{ccc}
m_p = 5.79 \cdot 10^{-2} \cdot m_e = 5.27 \cdot 10^{-32} & a_g = 9.77 \cdot 10^{-8} & T_{\text{Scale}} = 9.54 \cdot 10^{-12} \\
\gamma_0 = 0.95 & \gamma_2 = 6 & \gamma_r = 0.34 \\
g_R = 1.47 \cdot 10^{-3} & R = 4.88 \cdot 10^{-3} & P = 73.78
\end{array}$$

Table 4.2: Numerical values of physical parameters for the simulation of exciton-polariton condensates in the self-similar scaling regime

In contrast to the parameter regime discussed in the previous section, there is no need to tune the polariton mass to negative values in this case. This is because the first KPZ coefficient, $\nu = \frac{\gamma_2}{2} - \frac{4g_r}{R} = 1.795$, is inherently positive, resulting in stable phase dynamics in accordance with the KPZ equation. Regarding the spatially varying pumping, we used the same functional form as in the previous section 4.1, with parameters $L_0 = 370\mu m$ and $\sigma = 38.8\mu m$. All simulations in this section were conducted with a lattice consisting of 8192 lattice sites. In this section we have used a larger grid than in the previous section, which was made possible by increasing the timestep size. An illustration of a single run extended to $t_{\max} = 100$ns is shown in Fig. 4.8. In this plot it becomes apparent that some defects emerge in the early stages of the simulation and subsequently propagate in both the density and phase representations of the condensate. In order to obtain a clean real-time image of the phase evolution, we need to eliminate the static phase rotation introduced by the chemical potential μ. This rapid phase rotation effectively obscures the phase dynamics, making it difficult to analyse the emerging structures. To address this,

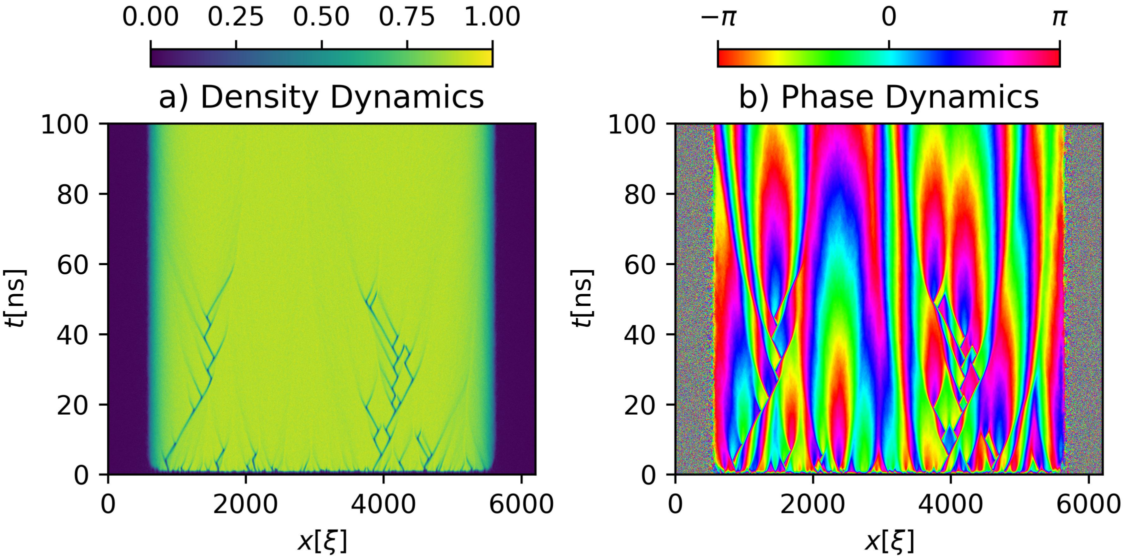

Figure 4.8: Real space representation of polariton condensate dynamics with scattering rate $R = 4.88 \cdot 10^{-3}$ evolving to a maximum propagation time of 100 ns: a) Depicts the density dynamics normalised to the maximum density. Emerging defects manifest as dark lines in the evolution plot. b) Shows the time evolution of the phase, where the defects are also visible as continuous lines representing constant phase values.

we perform a subtraction process by unwrapping the phase evolution at an arbitrary lattice point. Subsequently, we fit a linear function to this phase data. The slope of this linear function corresponds directly to the chemical potential μ. According to the formula 2.31, in numerical units the chemical potential of a polariton condensate within the KPZ regime is expected to be:

$$\mu = \omega_0 = 2\frac{g_R\gamma_0}{R} = 0.573 \tag{4.4}$$

This value is reasonably close to our simulation result, which is approximately 0.575. The small deviation can be attributed to phase fluctuations stemming from the initial noise introduced by the TWA method and from phase jumps induced by the propagating defects.

Once the chemical potential has been determined, we can use the following formula to calculate the healing length of the condensate:

$$\xi = \frac{1}{\sqrt{2m_p\mu}} \tag{4.5}$$

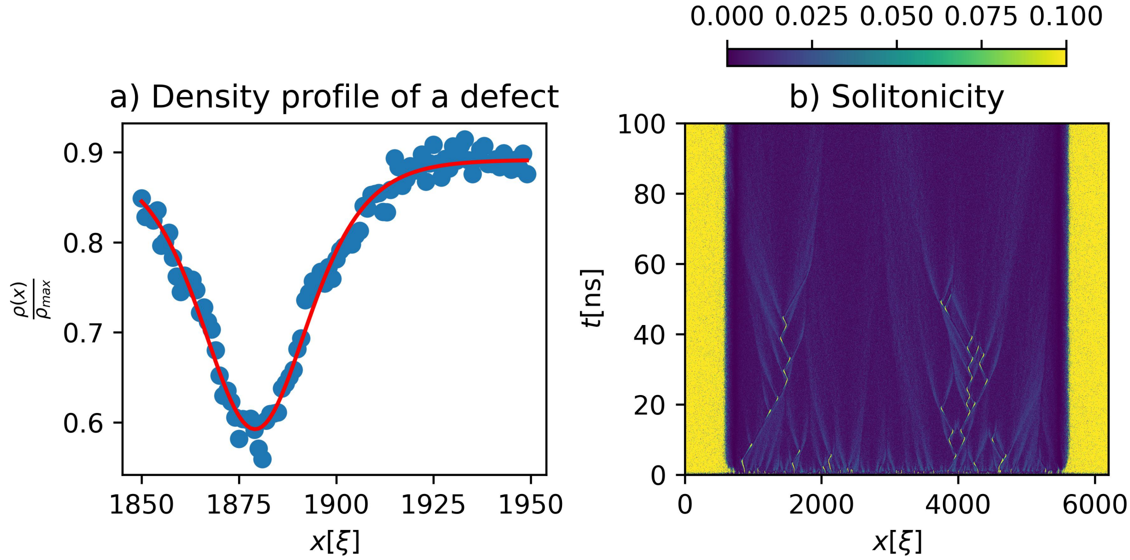

Figure 4.9: Analysis of emerging defects in a condensate with scattering rate $R = 4.88 \cdot 10^{-3}$ evolving to 100 ns: a) Demonstrates the fitting of the typical density profile of a dark soliton, as described in Equation 4.2, to the density dip associated with a defect. b) Presents a plot of solitonicity $S(t,x) = |\rho_0 - \rho(t,x)||\partial_x \theta(t,x)|$, an observable that measures the simultaneous occurrence of a phase jump and a density dip. This plot matches the defects shown in Figure 4.8, providing strong evidence to classify these defects as dark solitons.

Consequently, we obtain a value of approximately 1.32 in units of lattice points for the healing length in our simulation.

We once again analyse the emerging defects, focusing on the profile of the density dip created by these defects. Interestingly, the classical soliton shape as defined in Equation 4.2 fits the density profile of the dip remarkably well (see Figure 4.9 a)). It is interesting to note that from this fit we can extract a new healing length corresponding to approximately 20 grid points. We therefore conclude that these defects introduce an additional length scale into the system.

As in our previous analysis, to classify these defects as dark solitons we need to show that the density dip coincides with a phase jump. To achieve this, we examine the solitonicity operator defined in Equation 4.3. In Figure 4.9 we observe that regions of high solitonicity align precisely with the positions of the defects, providing compelling evidence to label these defects as dark solitons.

The propagation behaviour of these dark solitons differs significantly from the solitons studied in the previous section. Here, the solitons travel along straight lines

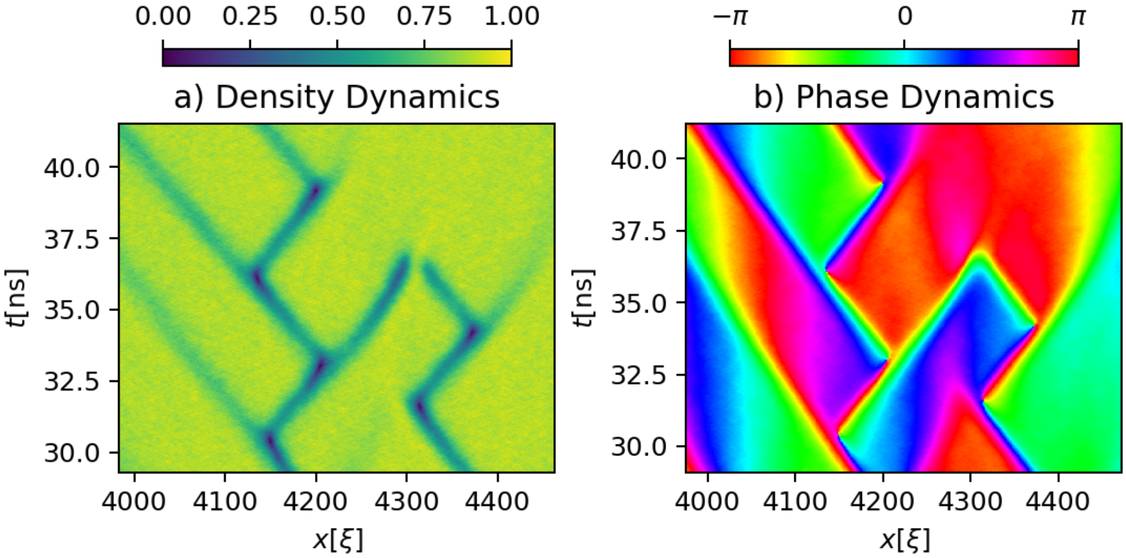

Figure 4.10: Detailed study of the right soliton branch in Fig. 4.8: a) In the density plot we observe the splitting of a single soliton into two distinct entities, marked by a density minimum at the split point (see e.g. minimum at $t = 33$ns). b) In the phase plot, vortex-like structures emerge at these splitting points. However, it is worth noting that the phase doesn't change continuously, but changes rapidly in the direction of the dominant daughter soliton, while remaining constant elsewhere.

until they reach vertex points where the density reaches its minimum and the solitons split into two distinct entities. Over time, this splitting process produces a pattern reminiscent of a root structure.

In Figure 4.10 we provide a close-up view of the right branch, focusing on a series of vertex points. An examination of the phase dynamics reveals that, as in the previous section, the multiple phase jumps at the splitting points give rise to vortex-like structures. These structures undergo a 2π phase change when encircling the core. However, unlike the previous space-time vortices, the traversal of the phase colour scale in this case is not continuous, but is characterised by a larger constant part and a smaller part where it changes rapidly. This observation suggests that the first vortices were the result of symmetric two-soliton collisions, whereas these vortices arise from an unsymmetric decay of a single soliton into two solitons.

Apart from the interesting defect dynamics, the evolution of the condensate may not appear to differ fundamentally from the parameter regime previously studied. However, the differences arise when we look for signs of self-similar scaling behaviour, which could potentially indicate the presence of a non-thermal fixed point. To this

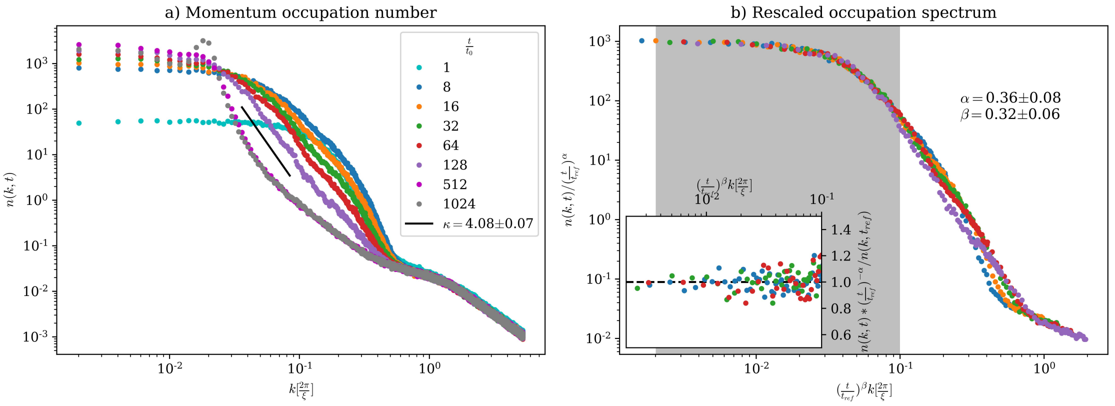

Figure 4.11: Evidence for self-similar scaling in the occupation spectrum: In plot a) the momentum occupation number at different time points is shown. It undergoes a shift from an initial box-shaped distribution to one that follows a power law with an negative exponent of $\kappa = 4.08$. On the right, we rescale these spectra relative to a reference time, $\frac{t_{\text{ref}}}{t_0} = 16$. It is noticeable that the spectra are closely aligned, especially in the infrared (IR) region. Through a fitting process we derive the rescaling exponents: $\alpha = 0.36$ and $\beta = 0.32$. The inset shows the ratio of the rescaled spectra compared to the reference spectra, with a random distribution around 1, as expected for self-similar scaling. These occupancy spectra represent the average results of 170 simulation runs at a scattering rate of $R = 4.88 \cdot 10^{-3}$, with the latest time point corresponding to the maximum simulation time, $t_{\text{max}} = 800\text{ns}$.

end, we examine the momentum occupation number at different points in time. The collection of this spectrum requires several simulation runs of the same configuration. In Fig. 4.11 we show the momentum occupation spectrum resulting from a total of 170 runs. A substantial transformation can be observed in the momentum distribution, which initially exhibits a box-like shape but gradually evolves into a flatter profile, as clearly shown in the log-log plot of Fig. 4.11. This transformation is a strong indication of scaling behaviour. At the specific time $\frac{t}{t_0} = 128$, the momentum occupancy has fully developed its power law behaviour, characterised by a negative exponent of $\kappa = 4.08$. This result is particularly noteworthy as one would typically expect κ to be approximately 2 in one spatial dimension, in line with previous propositions [37] and findings in other one-dimensional systems [3]. However, as time progresses, the scaling behaviour stops and the power-law form disappears, indicating that the system has moved away from the vicinity of the non-thermal fixed point.

To confirm the self-similar nature of this scaling behaviour, we performed a rescaling of the spectra with respect to a chosen reference time, denoted as $t_{\text{ref}} = 16t_0 = 12.5$ns. This rescaling was performed according to the functional form given by the Equation 2.4. Specifically, we scaled the momentum on the x-axis by $(\frac{t}{t_{\text{ref}}})^{\beta}$ and the occupation number by $(\frac{t}{t_{\text{ref}}})^{-\alpha}$. The resulting graph, shown in plot b) of Figure 4.11, clearly demonstrates that the occupation spectra at different time points in the IR region are in good agreement. This confirmation is further strengthened by examining the relative deviation of the spectra from the reference spectra, as shown in the inset. Here we observe only a slight divergence, mainly at higher momenta.

Taken together, these results provide compelling evidence that we have indeed uncovered a self-similar scaling phenomenon, as discussed in section 2.4. This observation strongly suggests the existence of a non-thermal fixed point. Remarkably, the scaling exponents α and β are very close to $\frac{1}{3}$, which is in line with our expectations given that we are operating in a regime where the phase fluctuations are governed by the KPZ equation (see [21] for more details). For a one-dimensional system, the equality of the scaling exponents is expected, reflecting the particle number conservation in the IR. In our case these exponents are indeed almost equal within the margin of error.

By making small adjustments to the parameters of our simulations, we can change both the number of solitons and their lifetime. In particular, the value of the scattering rate, denoted 'R', plays a key role in shaping the simulation results. This influence is clearly illustrated in Figure 4.12, which shows a simulation run with a slight reduction in the scattering rate. In this scenario there is a noticeable increase in the number of solitons compared to previous runs. Previous research, in particular studies on two-dimensional Bose-Einstein condensates near the Berezinskii-Kosterlitz-Thouless (BKT) transition, has provided insights into the substantial influence of vortices or defects in general on the scaling behaviour of a system. For example, in [26], the system was found to have a reduced scaling exponent of $\beta = 0.2$, which differs from the expected value of 0.5 [24] for such a system.

In the context of the polariton system, we encounter an interesting trade-off driven by the increased condensate activity in the form of numerous solitons. The lower the scattering rate R and therefore the higher the number of solitons, the more the condensate loses its characteristic property of self-similar scaling. This deviation is illustrated in Figure 4.13, which shows the momentum occupation spectrum for a simulation run with a reduced scattering rate of $R = 4.4 \cdot 10^{-3}$. The overlap of

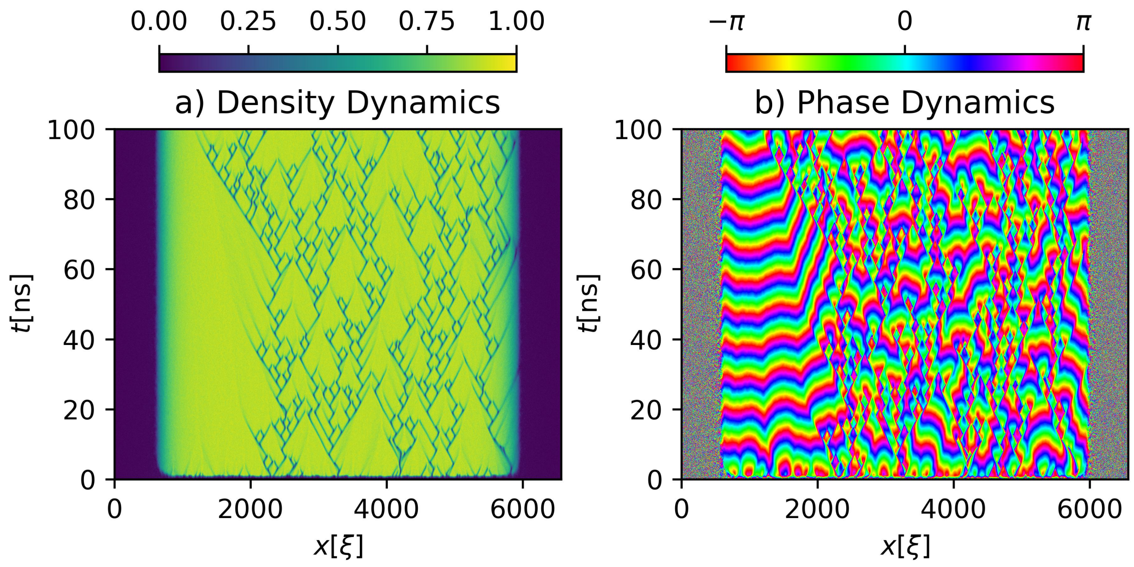

Figure 4.12: Real space representation of a simulation with a slightly reduced scattering rate ($R = 4.4 \cdot 10^{-3}$) compared to Figure 4.8. Notably, there is a significant increase in both the number of solitons and their lifetime. The simulation was performed with a maximum propagation time of 100 ns.

the occupancies at different times suggests the absence of scaling within the system. Consequently, this deviation implies a shift away from the vicinity of a non-thermal fixed point. On the contrary, reducing the number of solitons by increasing the scattering rate leads to an enhancement of the scaling behaviour. In Figure 4.14 we show the averaged momentum spectra derived from 170 simulation runs with an increased scattering rate of $R = 5.3 \times 10^{-3}$. Remarkably, a distinct power-law shape appears as early as $\frac{t}{t_0} = 64$ and persists until the last time points at 800 ns, where the scaling phenomenon finally ceases. The negative exponent of this power law, measured at $\kappa = 6.74$, exceeds the previous value, emphasising its dependence on factors such as the scattering rate and possibly other system parameters.

The scaling exponents, again close to $\frac{1}{3}$, now show slightly larger error bars. This slight increase in error is probably due to the wider momentum range used to rescale the spectra, as shown by the grey area in Figure 4.14 b). However, the extended fitting range should compensate for this increase in error, ensuring the reliability of our results.

To confirm that the enhanced scaling behaviour is associated with a reduced number of solitons, we examine the real-space representation of a simulation run used to generate the spectrum in Figure 4.14. In Figure 4.15 it becomes clear that simulations

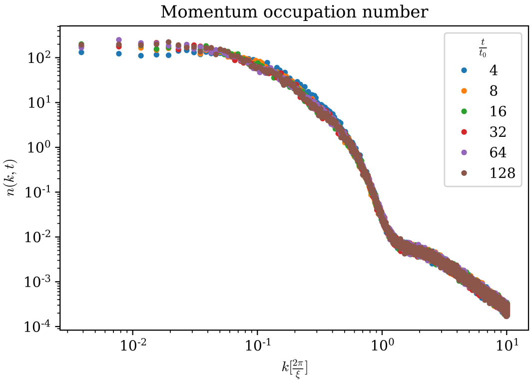

Figure 4.13: Occupation numbers in momentum space at different times: The occupancies at different time points overlap, indicating the absence of scaling in the system and a departure from the non-thermal fixed point. These spectra are derived from the averaging of 50 simulation runs, similar to the one seen in Figure 4.12, with a maximum propagation time of 100 ns and a scattering rate of $R = 4.4 \cdot 10^{-3}$.

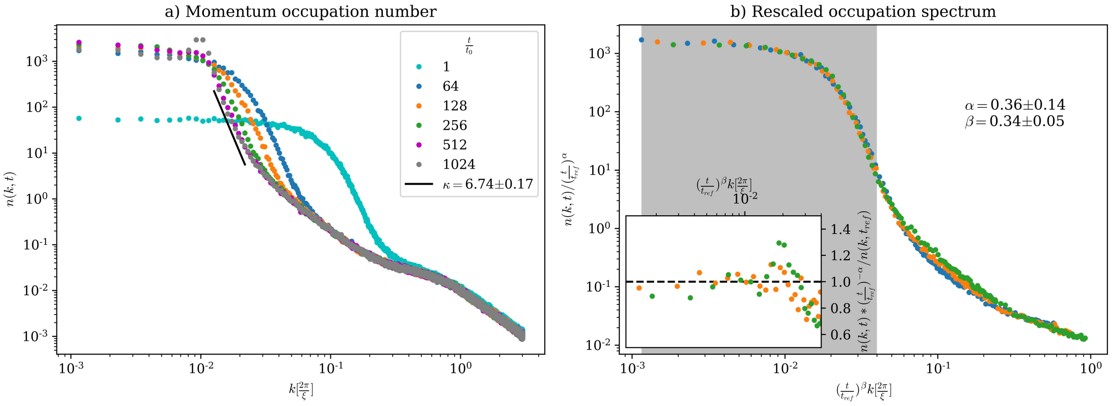

Figure 4.14: Evidence for self-similar scaling in the occupation spectrum: In plot a) the momentum occupation number at different time points is shown. It undergoes a shift from an initial box-shaped distribution to one that follows a power law with an negative exponent of $\kappa = 6.74$. On the right, we rescale these spectra relative to a reference time, $\frac{t_{\text{ref}}}{t_0} = 64$. Through a fitting process we derive the rescaling exponents: $\alpha = 0.36$ and $\beta = 0.34$. The inset shows the ratio of the rescaled spectra compared to the reference spectra, with a mostly random distribution around 1, as expected for self-similar scaling. Only at high momenta discrepencies arise most likely due to a increased fitting range as indicated by the grey area. These occupancy spectra represent the average results of 170 simulation runs at a scattering rate of $R = 5.3 \cdot 10^{-3}$, with the latest time point corresponding to the maximum simulation time, $t_{\text{max}} = 800$ns.

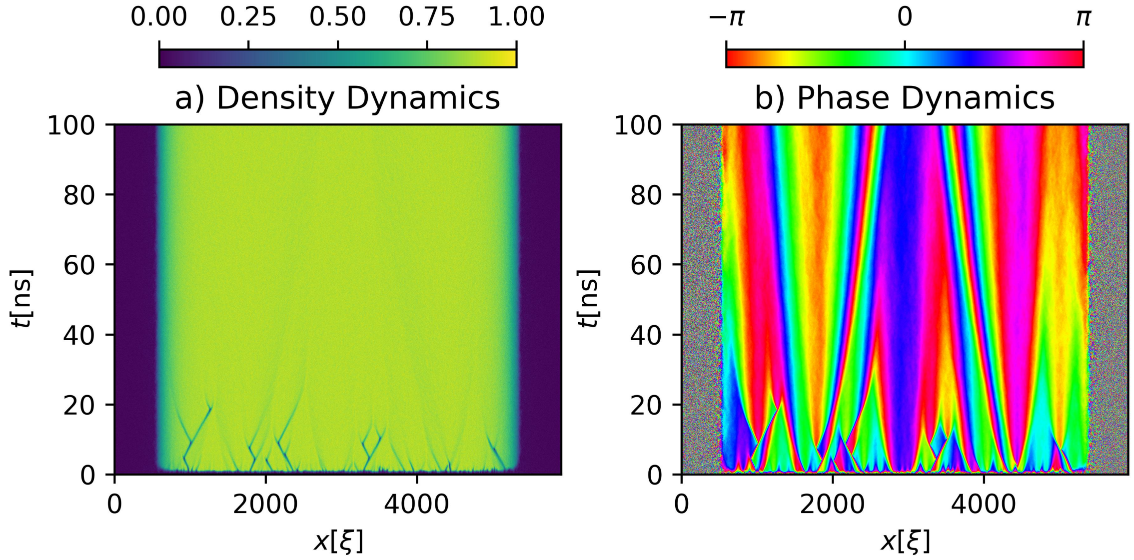

Figure 4.15: Real space representation of a simulation carried out with a slightly increased scattering rate ($R = 5.3 \times 10^{-3}$), in contrast to Figure 4.8. It can be observed that the solitons have significantly shorter lifetimes, resulting in fewer instances of splitting and an overall reduced presence of solitons in the system. The simulation covered a maximum propagation time of 100 ns.

with a scattering rate of $R = 5.3 \times 10^{-3}$ do indeed produce solitons that persist for shorter periods of time. This observation suggests two critical implications: first, that changes in the scattering rate significantly affect the lifetimes of the solitons, which in turn affects both their splitting frequency and consequently the total number of solitons present in the system at any given time. Secondly, it implies that the scaling behaviour, in particular the emergence of the power-law shape, tends to manifest itself after the solitons have dissipated from the system.

These results highlight the significant influence of solitons on the dynamics of polariton condensates. Furthermore, they suggest the possibility of observing similar scaling behaviour in regimes with numerous solitons, provided that sufficient time is provided for their eventual disappearance. Investigating such scenarios would require considerable computational resources, but could be an interesting focus for future studies.

5 Conclusion

In this thesis we have investigated the one-dimensional polariton condensate coupled to an exciton reservoir through the lens of numerical simulations. Our approach was based on the application of the split-step Fourier algorithm for time integration, complemented by the truncated Wigner approximation to capture essential quantum effects. Both methods were introduced in chapter 3 of this thesis. Amidst the vast parameter space, we have deliberately restricted our investigation to two distinct parameter regimes where the condensate exhibits stability and interesting pattern dynamics.

We used the values given in [9] for our simulation of the first parameter regime. Although we did not replicate the vortex-antivortex pairs documented in that work, our investigations revealed the emergence of propagating defects in both density and phase evolution. Upon closer examination, these defects exhibited density profiles similar to dark solitons. Structures with a phase winding of 2π around a core, which we identified as space-time vortices, appeared at the intersections of these dark solitons. This discovery led us to speculate that space-time vortices arise from symmetric collisions of two solitons. Furthermore, the absence of scaling, suggesting that there is no non-thermal fixed point to guide the time evolution of the condensate, was observed by checking the occupation number in momentum space. It is also possible that the dynamics are still dominated by early chaotic behaviour, in which case it would be desirable to run longer simulations, a task that is numerically very costly and therefore the subject of future work.

Subsequently, in section 4.2 we ventured into a different parameter regime characterised by a scaling behaviour. We first verified that we were operating within a regime where phase fluctuations follow the KPZ equation. To this end, we extracted the chemical potential associated with the stationary phase rotation of the polariton condensate and confirmed its agreement with the theoretical predictions described in section 2.5.

Examining the real-space representation of the condensate, we again detect the appearance of defects in the density and phase evolution of the condensate. We demonstrate that the density profile of these defects closely matches that of a dark soliton, and that the dip in density of the defect coincides with a phase jump, using the same analyses as in the previous section. Having identified these defects as solitons, we proceed to study the intersections where these solitons merge. At these intersections we observe a singular soliton splitting into two separate entities. During this process we again encounter vortex-like structures. However, due to the asymmetric nature of the decay process, the phase winding around the core does not exhibit a continuous rotation over 2π, but rather occurs over a small angle before remaining constant for the remainder of the arc. The repeated splitting of the solitons results in a branched soliton network that resembles a root structure.

During our analysis of the momentum occupation spectra, we discovered a characteristic scaling phenomenon. Initially, we observed a box-like distribution, which later evolved into a power law decay shape. Remarkably, it correlated strongly with the lifetimes of the solitons emerging in the system. By tuning the scattering rate R, we were able to manipulate both the number of solitons present at any time and the scaling characteristics. At higher scattering rates, corresponding to shorter soliton lifetimes, we observed a distinct scaling behaviour and a pronounced power-law decay. The exponent of this power law depended on R and ranged from about 4 to 7. This observation is in agreement with the results of a recent study by Vercesi et al. [38] as well as older reports [39, 40], where similarly high exponents were reported in soliton-rich polariton condensates.

Conversely, at lower scattering rates we found that the scaling behaviour ceased and the occupation number spectra converged. This striking observation raises questions about the underlying dynamics and the role of the scattering rate in shaping the scaling behaviour. One possible explanation could be the existence of multiple fixed points. The specific fixed point approached by a system as it evolves may be determined not only by its universality class, but also by certain system parameters. This explanation could be an interesting focus for further theoretical work on the concept of non-thermal fixed points.

Furthermore, it is worth noting that the scaling persists even after the solitons have decayed, suggesting that the infrared (IR) length scale is not solely determined by the coarsening length scale between defects. Instead, it appears that the background itself exhibits scaling behaviour. This phenomenon becomes even more interesting when considering that the solitons eventually merge with the background over time, which is best seen in the solitonicity plot 4.9. In particular, this plot shows filaments of solitonicity emanating from decaying solitons and being absorbed by the background. It is therefore possible that there is a transition from solitonic defects to background excitations, similar to sound waves, which may drive the observed scaling. Future research could start here to learn more about the interplay between scaling and defects.

To confirm the self-similarity of the scaling phenomenon, we rescaled the occupation spectra with respect to a reference time and found only small deviations. As predicted for a system associated with KPZ dynamics [21], the scaling exponents we extracted from the rescaling procedure were close to $\frac{1}{3}$.

This result paves the way for exciting future research exploring the connection between the KPZ equation and the Sine-Gordon model. Ongoing, unpublished work within Prof Gasenzer's research group has suggested similar scaling exponents when simulating the Sine-Gordon model. The presence of space-time vortices in both theories further supports the idea of a link between them. While there are already studies demonstrating a connection through a two-point correlation function between the Sine-Gordon model and the KPZ equation in the non-relativistic limit [41], a more formal investigation is required to strengthen this connection. Such an investigation may also reveal connections in the dynamics of the related condensate systems.

A Lists

A.1 List of Figures

A.2 List of Tables

B Bibliography

[1] Boris Nowak et al. *Non-thermal fixed points: universality, topology, & turbulence in Bose gases.* 2013. arXiv: `1302.1448 [cond-mat.quant-gas]`.

[2] Jürgen Berges, Alexander Rothkopf, and Jonas Schmidt. “Nonthermal Fixed Points: Effective Weak Coupling for Strongly Correlated Systems Far from Equilibrium”. In: *Phys. Rev. Lett.* 101 (4 July 2008), p. 041603. DOI: `10.1103/PhysRevLett.101.041603`. URL: `https://link.aps.org/doi/10.1103/PhysRevLett.101.041603`.

[3] Christian-Marcel Schmied et al. “Bidirectional universal dynamics in a spinor Bose gas close to a nonthermal fixed point”. In: *Phys. Rev. A* 99 (3 Mar. 2019), p. 033611. DOI: `10.1103/PhysRevA.99.033611`. URL: `https://link.aps.org/doi/10.1103/PhysRevA.99.033611`.

[4] Christian Marcel Schmied. “Universal Scaling Dynamics at Non-thermal Fixed Points in Multi-Component Bose Gases Far from Equilibrium”. PhD thesis. Heidelberg University, 2020.

[5] Sebastian Erne et al. “Universal dynamics in an isolated one-dimensional Bose gas far from equilibrium”. In: *Nature* 563.7730 (2018), pp. 225–229. ISSN: 1476-4687. DOI: `10.1038/s41586-018-0667-0`. URL: `http://dx.doi.org/10.1038/s41586-018-0667-0`.

[6] Maximilian Prüfer et al. “Observation of universal dynamics in a spinor Bose gas far from equilibrium”. In: *Nature* 563.7730 (2018), pp. 217–220. ISSN: 1476-4687. DOI: `10.1038/s41586-018-0659-0`. URL: `http://dx.doi.org/10.1038/s41586-018-0659-0`.

[7] J. Berges et al. “Turbulent thermalization process in heavy-ion collisions at ultrarelativistic energies”. In: *Phys. Rev. D* 89 (7 Apr. 2014), p. 074011. DOI: `10.1103/PhysRevD.89.074011`. URL: `https://link.aps.org/doi/10.1103/PhysRevD.89.074011`.

[8] J. Berges. *Nonequilibrium Quantum Fields: From Cold Atoms to Cosmology.* 2015. arXiv: `1503.02907 [hep-ph]`.

[9] Quentin Fontaine et al. "Observation of KPZ universal scaling in a one-dimensional polariton condensate". In: (2022). URL: https://doi.org/10.48550/arXiv.2112.09550.

[10] Albert Einstein. "Quantentheorie des einatomigen idealen Gases". In: *Königliche Preußische Akademie der Wissenschaften. Sitzungsberichte* (July 10, 1924), pp. 261–267. URL: https://www.uni-muenster.de/imperia/md/content/physik_ap/demokritov/mbecfornonphysicists/einstein_1924_1925.pdf.

[11] M. H. Anderson et al. "Observation of Bose-Einstein Condensation in a Dilute Atomic Vapor". In: *Science* 269.5221 (1995), pp. 198–201. DOI: 10.1126/science.269.5221.198. eprint: https://www.science.org/doi/pdf/10.1126/science.269.5221.198. URL: https://www.science.org/doi/abs/10.1126/science.269.5221.198.

[12] K. B. Davis et al. "Bose-Einstein Condensation in a Gas of Sodium Atoms". In: *Phys. Rev. Lett.* 75 (22 Nov. 1995), pp. 3969–3973. DOI: 10.1103/PhysRevLett.75.3969. URL: https://link.aps.org/doi/10.1103/PhysRevLett.75.3969.

[13] S. A. Moskalenko and D. W. Snoke. *Bose-Einstein Condensation of Excitons and Biexcitons: And Coherent Nonlinear Optics with Excitons*. Cambridge University Press, 2000. DOI: 10.1017/CBO9780511721687.

[14] K. Lagoudakis. *The Physics of Exciton-Polariton Condensates*. Physics. EPFL Press, 2013. ISBN: 9782940222759. URL: https://books.google.de/books?id=QakGDQAAQBAJ.

[15] J. Kasprzak et al. "Bose-Einstein condensation of exciton polaritons". English. In: *Nature* 443.7110 (July 2006), pp. 409–414. ISSN: 0028-0836. DOI: 10.1038/nature05131.

[16] Franco Dalfovo et al. "Theory of Bose-Einstein condensation in trapped gases". In: *Rev. Mod. Phys.* 71 (3 Apr. 1999), pp. 463–512. DOI: 10.1103/RevModPhys.71.463. URL: https://link.aps.org/doi/10.1103/RevModPhys.71.463.

[17] Philipp Heinen. "Phase Correlators in Gross-Pitaevskii Systems Far from Equilibrium". MA thesis. Heidelberg University, 2020.

[18] Alexander Altland and Ben D. Simons. *Condensed Matter Field Theory*. 2nd ed. Cambridge University Press, 2010. DOI: 10.1017/CBO9780511789984.

[19] Boris Nowak et al. “Nonthermal fixed points, vortex statistics, and superfluid turbulence in an ultracold Bose gas”. In: *Phys. Rev. A* 85 (4 Apr. 2012), p. 043627. DOI: `10.1103/PhysRevA.85.043627`. URL: `https://link.aps.org/doi/10.1103/PhysRevA.85.043627`.

[20] Ido Siovitz. “Topological Excitations and Universal Scaling of the One-Dimensional Spin-1 Bose-Einstein Condensate Far from Equilibrium”. MA thesis. Heidelberg University, 2022.

[21] Quentin Fontaine et al. “Kardar–Parisi–Zhang universality in a one-dimensional polariton condensate”. In: *Nature* 608.7924 (Aug. 2022), pp. 687–691. DOI: `10.1038/s41586-022-05001-8`. URL: `https://doi.org/10.1038%2Fs41586-022-05001-8`.

[22] Iacopo Carusotto. *Quantum Fluids of Light.* 2022. DOI: `10.48550/ARXIV.2211.10980`. URL: `https://arxiv.org/abs/2211.10980`.

[23] Maximilian Prüfer et al. “Observation of universal dynamics in a spinor Bose gas far from equilibrium”. In: *Nature* 563.7730 (Nov. 2018), pp. 217–220. DOI: `10.1038/s41586-018-0659-0`. URL: `https://doi.org/10.1038%2Fs41586-018-0659-0`.

[24] Asier Piñeiro Orioli, Kirill Boguslavski, and Jürgen Berges. “Universal self-similar dynamics of relativistic and nonrelativistic field theories near nonthermal fixed points”. In: *Physical Review D* 92.2 (July 2015). DOI: `10.1103/physrevd.92.025041`. URL: `https://doi.org/10.1103%2Fphysrevd.92.025041`.

[25] Mehran Kardar, Giorgio Parisi, and Yi-Cheng Zhang. “Dynamic Scaling of Growing Interfaces”. In: *Phys. Rev. Lett.* 56 (9 Mar. 1986), pp. 889–892. DOI: `10.1103/PhysRevLett.56.889`. URL: `https://link.aps.org/doi/10.1103/PhysRevLett.56.889`.

[26] Markus Karl and Thomas Gasenzer. “Strongly Anomalous Non-thermal Fixed Point in a Quenched Two-dimensional Bose Gas”. In: *New Journal of Physics* 19.9 (2017), p. 093014. ISSN: 1367-2630. DOI: `10.1088/1367-2630/aa7eeb`. URL: `http://dx.doi.org/10.1088/1367-2630/aa7eeb`.

[27] Markus Karl, Boris Nowak, and Thomas Gasenzer. “Universal Scaling at Non-thermal Fixed Points of a Two-component Bose Gas”. In: *Physical Review*

A 88.6 (2013). ISSN: 1094-1622. DOI: 10.1103/physreva.88.063615. URL: http://dx.doi.org/10.1103/PhysRevA.88.063615.

[28] Christopher D. Mink et al. “Variational truncated Wigner approximation for weakly interacting Bose fields: Dynamics of coupled condensates”. In: *SciPost Phys.* 12 (2022), p. 051. DOI: 10.21468/SciPostPhys.12.2.051. URL: https://scipost.org/10.21468/SciPostPhys.12.2.051.

[29] Christian-Marcel Schmied. “Emergence of Structure in a Quenched (Quasi) One-dimensional Spin-1 Bose-Einstein Condensate in Comparison with Experiments”. MA thesis. Heidelberg University, 2016.

[30] Anatoli Polkovnikov. “Phase Space Representation of Quantum Dynamics”. In: *Annals of Physics* 325.8 (2010), pp. 1790–1852. ISSN: 0003-4916. DOI: 10.1016/j.aop.2010.02.006. URL: https://www.sciencedirect.com/science/article/pii/S0003491610000382.

[31] M. A. Hillery et al. “Distribution Functions in Physics: Fundamentals”. In: *Physics Reports* 106 (1984), pp. 121–167.

[32] Scott A. Sarra. “The Method of Characteristics with applications to Conservation Laws”. In: *Journal of Online Mathematics and its Applications* (2003).

[33] Ido Siovitz et al. *Universal dynamics of rogue waves in a quenched spinor Bose condensate*. 2023. arXiv: 2304.09293 [cond-mat.quant-gas].

[34] Aurélien Trichet et al. “Long-range correlations in a 97% excitonic one-dimensional polariton condensate”. In: *Phys. Rev. B* 88 (12 Sept. 2013), p. 121407. DOI: 10.1103/PhysRevB.88.121407. URL: https://link.aps.org/doi/10.1103/PhysRevB.88.121407.

[35] Katharina Rojan et al. “Enhanced Second-Order Nonlinearity for THz Generation by Resonant Interaction of Exciton-Polariton Rabi Oscillations with Optical Phonons”. In: *Phys. Rev. Lett.* 119 (12 Sept. 2017), p. 127401. DOI: 10.1103/PhysRevLett.119.127401. URL: https://link.aps.org/doi/10.1103/PhysRevLett.119.127401.

[36] Davide Squizzato, Léonie Canet, and Anna Minguzzi. “Kardar-Parisi-Zhang universality in the phase distributions of one-dimensional exciton-polaritons”. In: *Physical Review B* 97.19 (May 2018). DOI: 10.1103/physrevb.97.195453. URL: https://doi.org/10.1103%2Fphysrevb.97.195453.

[37] A. D. Rutenberg and A. J. Bray. "Unwinding Scaling Violations in Phase Ordering". In: *Phys. Rev. Lett.* 74 (19 May 1995), pp. 3836–3839. DOI: `10.1103/PhysRevLett.74.3836`. URL: `https://link.aps.org/doi/10.1103/PhysRevLett.74.3836`.

[38] Francesco Vercesi et al. *Phase diagram of one-dimensional driven-dissipative exciton-polariton condensates*. 2023. arXiv: `2307.15664 [cond-mat.stat-mech]`.

[39] Nataliya Bobrovska and Michał Matuszewski. "Adiabatic approximation and fluctuations in exciton-polariton condensates". In: *Phys. Rev. B* 92 (3 July 2015), p. 035311. DOI: `10.1103/PhysRevB.92.035311`. URL: `https://link.aps.org/doi/10.1103/PhysRevB.92.035311`.

[40] Liang He, Lukas M. Sieberer, and Sebastian Diehl. "Space-Time Vortex Driven Crossover and Vortex Turbulence Phase Transition in One-Dimensional Driven Open Condensates". In: *Phys. Rev. Lett.* 118 (8 Feb. 2017), p. 085301. DOI: `10.1103/PhysRevLett.118.085301`. URL: `https://link.aps.org/doi/10.1103/PhysRevLett.118.085301`.

[41] Pasquale Calabrese, Márton Kormos, and Pierre Le Doussal. "From the sine-Gordon field theory to the Kardar-Parisi-Zhang growth equation". In: *EPL (Europhysics Letters)* 107.1 (July 2014), p. 10011. DOI: `10.1209/0295-5075/107/10011`. URL: `https://doi.org/10.1209%2F0295-5075%2F107%2F10011`.

Erklärung:

Ich versichere, dass ich diese Arbeit selbstständig verfasst habe und keine anderen als die angegebenen Quellen und Hilfsmittel benutzt habe.

Heidelberg, den 9. Oktober 2023